



## Validation of the PALM model system 6.0 in real urban environment; case study of Prague-Dejvice, Czech Republic

Jaroslav Resler<sup>1</sup>, Kryštof Eben<sup>1</sup>, Jan Geletič<sup>1</sup>, Pavel Krč<sup>1</sup>, Martin Rosecký<sup>1</sup>, Matthias Sühling<sup>2</sup>, Michal Belda<sup>3</sup>, Vladimír Fuka<sup>3</sup>, Tomáš Halenka<sup>3</sup>, Peter Huszár<sup>3</sup>, Jan Karlický<sup>3</sup>, Nina Benešová<sup>4</sup>, Jana Ďoubalová<sup>4</sup>, Kateřina Honzáková<sup>4</sup>, Josef Keder<sup>4</sup>, Šárka Nápravníková<sup>4</sup>, and Ondřej Vlček<sup>4</sup>

<sup>1</sup>Institute of Computer Science, Czech Academy of Sciences, Prague, Czech Republic

<sup>2</sup>Institute of Meteorology and Climatology, Leibniz University Hannover, Hannover, Germany

<sup>3</sup>Faculty of Mathematics and Physics, Charles University, Prague, Czech Republic

<sup>4</sup>Czech Hydrometeorological Institute, Prague, Czech Republic

**Correspondence:** Jaroslav Resler (resler@cs.cas.cz)

**Abstract.** The PALM 6.0 model system has been rapidly developed in the recent years with respect to its capability to simulate physical processes within urban environments. In this regard, it includes e.g. energy-balance solvers for building and land surfaces, a radiative transfer model to account for multiple reflections and shading, as well as a plant-canopy model to consider the effects of plants on the (thermo)dynamics of the flow. This study provides a thorough evaluation of modelled meteorological, air chemistry and wall-surface quantities against dedicated in-situ measurements taken in an urban environment in Prague, Dejvice, Czech Republic. Measurements included e.g. monitoring of air quality and meteorology in street canyons, surface temperature scanning with infrared camera and monitoring of wall heat fluxes. Large-eddy simulations (LES) for multiple days within two summer and three winter episodes that are characterized by different atmospheric conditions were performed with the PALM model driven by boundary conditions obtained from a mesoscale model. For the simulated episodes, the resulting temperature, wind speed and concentrations of chemical compounds within street canyons agreed well with the observations, except the LES did not adequately capture nighttime cooling near the surface at certain meteorological conditions. In some situations, less turbulent mixing was modelled resulting in higher near-surface concentrations. At most of the surface evaluation points the simulated wall-surface temperature agreed fairly well with the observed one regarding its absolute value as well as daily amplitude. However, especially for the winter episodes and for modern buildings with multi-layer walls, the heat transfer through the wall is partly not well captured leading to discrepancies between the modelled and observed wall-surface temperature. Furthermore, we show that model results depend on the accuracy of the input data, particularly the temperatures of surfaces affected by nearby trees strongly depend on the spatial distribution of the leaf area density, land-surface temperatures at grass surfaces strongly depend on the initial soil moisture, or wall-surface temperatures depend on the correct prescription of wall material parameters, though these parameters are often not available with sufficient accuracy. Moreover, we also point out current model limitations, here we particularly focus on implications with respect to the discrete representation of topography on a Cartesian grid, complex heterogeneous facades, as well as glass facades that are not well represented in terms of radiative processes.

With these findings presented, we aim to validate the representation of physical processes in PALM as well as to point out spe-



cific shortcomings. This will help to build a baseline for future developments of the model and for improvements of simulations  
25 of physical processes in an urban environment.

## 1 Introduction

A large percentage of the world's population live in large cities (55 % as of 2018) and the percentage is expected to be growing  
(UN, 2019). In addition to that, global climate change, especially global temperature increase, will influence most natural  
ecosystems and human society with potentially severe impacts worldwide. The high level of attention currently being paid  
30 to the impact of climate change on urban areas is certainly legitimate and supported by many important studies and globally  
adopted reports (IPCC, 2014a, b). Moreover, intensified urbanization raises awareness that control of the microclimate in the  
urban environment is crucial for well-being of city inhabitants, as it can reduce heat stress and contribute to improvements  
of the living environment in cities. (Mutani and Fiermonte, 2017). The problem of increased heat stress in urban areas as  
a consequence of what has become known as the urban heat island (UHI) is therefore of direct concern to the municipal  
35 authorities being aware that the well-being of their inhabitants is vital, in many ways, to the well-being of the whole city.  
Moreover, UHI effect is often followed by secondary processes, e.g. air quality issues. Researchers have responded to, or  
anticipated, such concern about modelling of urban climate processes and various small-grid scale models and frameworks for  
(numerical) modelling have recently been developed (Geletič et al., 2018).

The health and well-being of the urban population is influenced by the conditions of the urban environment. The local  
40 microclimate, exposure to pollutants, as well as human comfort of the urban population depends strongly on the local conditions  
determined by the urban environment. Thereby, the turbulent flow, exchange of latent and sensible heat, as well as the radiative  
transfer processes play an important role and need to be considered in modelling approaches. Implementation of important  
microclimate processes (e.g. turbulence, heat fluxes or radiation) in street-level scale models is typically partially or fully  
parameterized. The most exhaustive approach consists of a group of computational fluid dynamics (CFD) models. The explicit  
45 simulation of turbulent flow is computationally demanding; thus, various techniques have to be adapted to make calculations  
feasible, usually based on limiting the range of the length scales and time scales of the turbulent flow to be resolved.

This study is using the PALM model system 6.0 (Maronga et al., 2020), which is an atmospheric modelling system. The core  
of the system contains model dynamics based on the LES (Large Eddy Simulation) and RANS (Reynolds-Averaged Navier-  
Stokes) techniques with additional modules for modelling of various atmospheric processes, e.g. interaction of atmosphere  
50 with earth surface or cloud microphysics. This system core is complemented with a rich set of *PALM-4U* (PALM for urban  
applications) modules related to modelling of physical phenomena relevant for urban climate, such as the interaction of solar  
radiation with urban surfaces and with urban vegetation, sensible and latent heat fluxes from the surfaces, storage of heat inside  
buildings and in pavements, or dispersion and chemical reaction of air pollutants (see Maronga et al., 2020). The first version  
of the PALM urban components represented the urban surface model (PALM-USM) which had been validated using data from  
55 a short experimental campaign in the centre of Prague (Resler et al., 2017). The new set of modules in PALM is more general  
and is divided according to the physical processes they cover. The most relevant for urban climate are the land surface model



(LSM), the building surface model (BSM), the radiative transfer model (RTM), and the plant-canopy model (PCM). The human biometeorology module (BIO) then allows to evaluate the impact of simulated climate conditions on human population.

Validation of the urban model requires a dataset of measurements of the urban meteorological and air quality conditions, properties of the urban canopy elements and of the energy exchange among parts of the urban canopy. Several campaigns of comprehensive observations and measurements of the urban atmospheric boundary layer covering more than one season were performed in the past. The Basel Urban Boundary Layer Experiment (BUBBLE) dataset containing observations from Basel is specifically targeted for validation of urban radiation models, urban energy balance models and urban canopy parameterizations (Rotach et al., 2005). The MUSE experiment (Montreal Urban Snow Experiment) aimed at the thermoradiative exchanges and the effect of snow cover in the urban atmospheric boundary layer (Lemonsu et al., 2008). The CAPITOU (Canopy and Aerosol Particles Interaction in TOulouse Urban Layer) project (Masson et al., 2008) concentrated on the role of aerosol particles in the urban layer.

Results of urban measurement campaigns have already been used for validation of several micrometeorological models, models of radiative transfer and microscale chemical transport models. Micro-scale model validation brings difficulties due to high heterogeneity of the urban environment and the studied quantities, due to uncertainty in the knowledge of the details of urban canopy properties as well as due to local irregularities caused by domain discretization. Important examples of such validation studies were published by Qu et al. (2013), Maggiotto et al. (2014) or Toparlak et al. (2015). Most often they analyze micrometeorological models of the RANS type. Early examples of LES validation studies that include thermal conditions within cities were presented by Nozu et al. (2008) and Liu et al. (2012). Due to our previous experience with limited validation of surface temperatures simulated by the PALM model (Resler et al., 2017), the aim of this study was to design a comprehensive experiment for complex model validation, including air velocity, air pollution or surface temperature analysis.

The main goal of this study was to compare detailed temporary and spatially localized observations with the results of the micro-scale PALM simulations in various urban canopy and meteorological conditions to assess the performance of the newly developed or updated PALM modules RTM, BSM, LSM, and PCM inside the complete modelling system. Additional purpose of this study was to assess the PALM model performance for its utilization in urbanistic studies. The results of this study serve for planning future improvements of the PALM model and its PALM-4U components as well as for improvements of the model inputs. These results also provide information which can improve the design of future validation campaigns.

These considerations also influenced the selection of the studied area. Prague-Dejvice quarter provides a typical urbanized area inside Prague and similar Central European cities with various types of urban environment. Further, the realization of the street level observation campaign was technically and organizationally easier in this area than e.g. in the historical centre of Prague. Moreover, this area represents one of the pilot areas for urban adaptations studies carried out in cooperation with Prague Municipality and their organizations (e.g. Prague Institute of Urban Planning and Development). The selection of this area was thus also influenced by their interest in the results of this study and their plan of subsequent modelling studies of urban heat island and air quality adaptation and mitigation strategies for this quarter.



90 Section 2 gives a detailed overview of the observation campaign, followed by a description of the numerical setup in Sect. 3. In Sect. 4 results from the numerical experiment and the observation campaign are presented and compared. Finally, Sect. 5 closes with a summary, outlines the current limitations of the model, and gives ideas for future improvements.

## 2 Observation campaign

The observation campaign was designed with two main aims: 1) to evaluate PALM with its newly developed or improved  
95 thermal modules - radiative transfer model (RTM), land and building surface modules (LSM, BSM), and plant canopy model (PCM) through its capability to reproduce surface temperatures; 2) to evaluate its capability to reproduce pollutant concentrations and meteorology values in different types of street canyons with special focus on the impact of trees in the streets on both quantities. The campaign was carried out in a warm part of the year (10–23 July 2018, further referred to as summer campaign) and a cold part of the year (23 November–10 December 2018, further referred to as winter campaign). Measurement locations  
100 are shown in Fig. 1 and measurements itself are described in Sect. 2.3.1–2.3.5. More details on the campaign are available in ČHMÚ (2020).

### 2.1 Study area

Study area is located in the north-west centre of Prague, capital city of the Czech Republic. The localization and map of this area is presented in Fig. S1 in supplements. This figure also marks the extent of the PALM modelling domains; for more  
105 information about model domain setup see Sect. 3.1. The studied area includes complex terrain mainly in the northern part of the outer domain, the altitudes range from up to 175 to 346 meters above sea level in the outer domain, variability of the inner domain is up to 30 m (see Fig. S2). The observations were located inside the inner domain (blue square in Fig. S2). This area is characterized as a densely built-up area with specific conditions created by the roundabout (Vítězné náměstí) in combination with south-east (Evropská / Čs. Armády) and south-north (Jugoslávských partyzánů / Svatovítská) oriented boulevards. East  
110 and partially south part of this domain represents a typical historical residential area in Prague-Dejvice with a combination of old and new buildings and a variety of other urban components (such as gardens, parks or parking places). North-west quarter is built up by buildings of the Czech Technical University campus. South-west and north-east parts of the domain are sparsely built-up by family houses. Local specifics include green intra-blocks with gardens and trees, usually with pervious surfaces; Prague historic centre usually has impervious intra-blocks. The building heights alongside the streets range approximately from  
115 20 to 30 m, the highest building in the domain is 60 m high. Both boulevards are approximately 40 m wide and do not contain much green vegetation, except for Jugoslávských partyzánů Street where high broadleaf trees ( $\pm 20$  m) are located. Majority of the trees are located in the intra-blocks and parks. Landcover map of the study area based on Urban Atlas 2012 geodatabase is shown in Fig. S3.

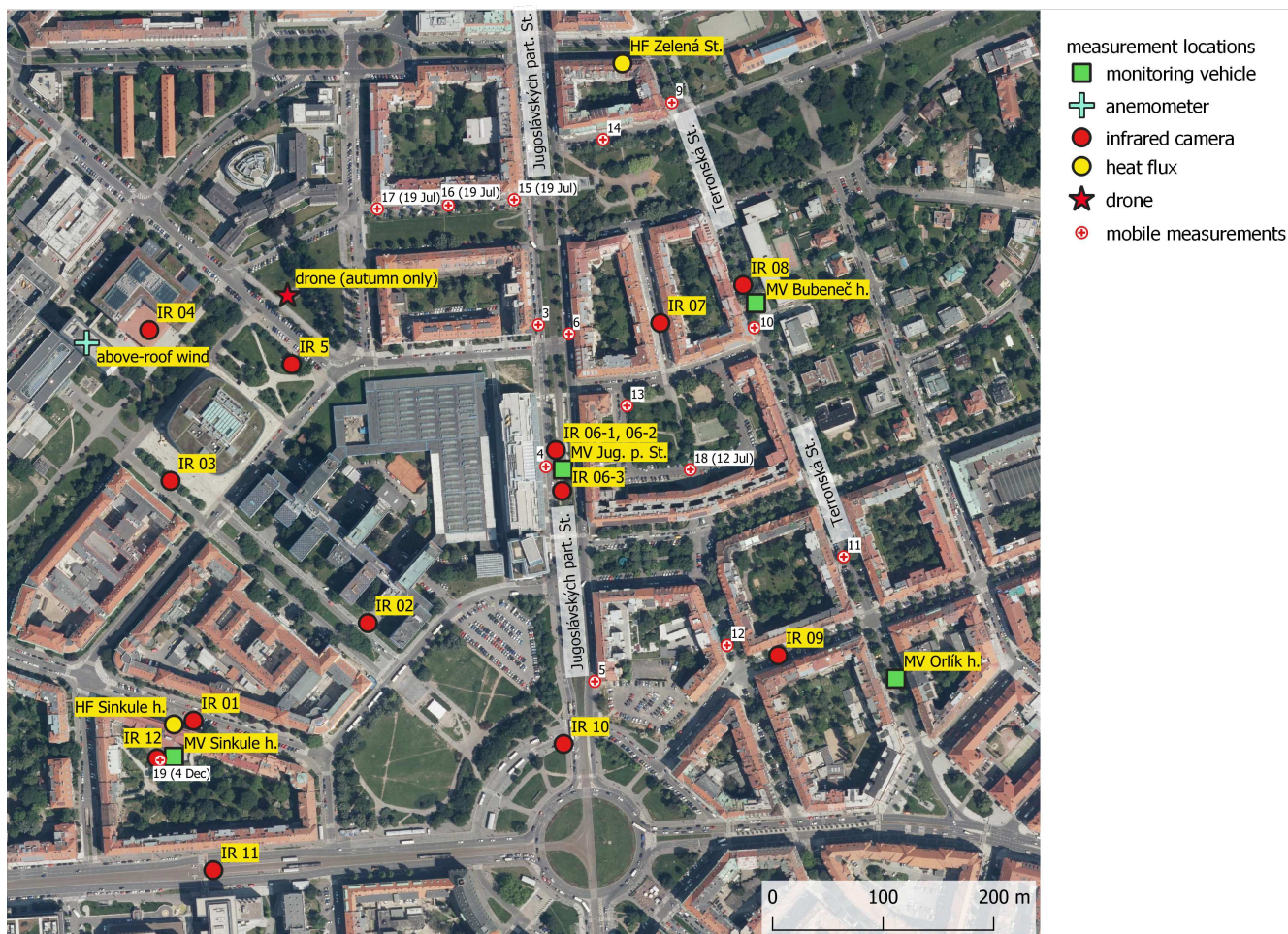


**Figure 1.** Map of measurement locations. Orthophoto was provided by WMS of the Czech Office for Surveying, Mapping and Cadastre (ČÚZK, 2020). For more information about point location (longitude, latitude etc.) see Table S1.

## 2.2 Validation episodes and synoptic situation

### 120 2.2.1 Summer campaign

The summer observation campaign ran for two weeks from 10 July 2018 to 23 July 2018 (see Table S2 in supplements) out of which two shorter episodes were selected for model simulations: 14–16 July (e1) and 19–23 July (e2). Synoptically, the weather was influenced by a high pressure ridge over Central Europe between an Icelandic low and an Eastern Europe low-pressure system for most of the summer campaign. Daily maximum temperature as measured at the Praha-Karlov (WMO ID 11519) station was below 30°C for the entire period with the exception of 21 July when the maximum temperature reached 31.2°C. The beginning of the period was partially cloudy, mostly with altostratus clouds forming in the morning and early afternoon



on 19 July. The period between afternoon on 19 July and late afternoon on 21 July was mostly clear with cirrus clouds. End of the 21 July was cloudy, mostly with low-level cumulus. Important solar parameters mid-episode (19 July 2018) were: time of sunrise at 03:13 UTC, time of sunset at 19:02 UTC and solar noon at 11:08 UTC.

## 130 2.2.2 Winter campaign

The winter part of the observation campaign lasted from 24 November 2018 to 10 December 2018 (see Table S3 in supplements) and for the purposes of model validation, three episodes were selected: 24–26 November (e1), 27–29 November (e2) and 4–6 December (e3). Weather was influenced by a typical late autumn synoptical situation with westerly flow and low-pressure systems and a series of fronts separated by two anticyclonic situations (27–29 November and 5 December). During  
135 the campaign several occluded frontal passages were recorded in Prague: 24, 30 November and 2, 3, 4 and 6 December with rainfall on 30 November (4.3 mm at Praha-Ruzyně station; WMO ID 11518) and 2 and 3 December (9.8 mm and 3.6 mm at Praha-Ryzuně station). Average daily temperatures ranged from  $-4^{\circ}\text{C}$  on 29 November to  $9^{\circ}\text{C}$  on 3 December 2018. Average daily wind speed was around  $3\text{ m}\cdot\text{s}^{-1}$  except for 26 November when it reached  $4.4\text{ m}\cdot\text{s}^{-1}$  and then 4–6 December with daily values of 4.8, 6.0 and  $5.7\text{ m}\cdot\text{s}^{-1}$ . Important parameters of the solar radiation daily cycle in Prague were (as of 1 December  
140 2018): sunrise at 6:39 UTC, sunset at 15:02 UTC, solar noon at 10:51 UTC.

## 2.3 Observed quantities and equipment used

### 2.3.1 Infra-red camera measurements

Surface temperature measurements by the infrared (IR) camera were carried out for two days (45 hours) and 3 days (50 hours) during the summer and winter campaign respectively (see Table S2 and Table S3). Measurements were performed at  
145 twelve locations shown in Fig. 1 approximately every 60–80 minutes. At each location, several directions were chosen and usually two snapshots capturing horizontal (grounds) and vertical (walls) surfaces were taken in each direction. We use the following nomenclature further in the text: <location\_number>-<direction\_number>-H/V. For example 02-1\_H means image of the ground taken from the second location in the first direction. In every image, a few evaluation points labeled by numbers were chosen and temperature time series extracted. The particular point at which modelled and observed values are compared  
150 is then referred to e.g. as 02-1\_H3. The observation campaign in total gathered time series of surface temperature for 66 ground and 73 wall evaluation points representing various surface types in order to evaluate model performance under different surface parameter settings (e.g. different surface materials and conditions).

Temperature was measured by the FLIR SC660 (FLIR, 2008) - the same camera that was used in Resler et al. (2017). As already described in the cited article, the camera's thermal sensor has a field of view of 24 by  $18^{\circ}$  and a spatial resolution (given  
155 as an instantaneous field of view) of 0.65 mrad. The spectral range of the camera is 7.5 to  $13.0\ \mu\text{m}$ , and the declared thermal sensitivity at  $30^{\circ}\text{C}$  is 45 mK. The measurement accuracy for an object with a temperature between 5 and  $120^{\circ}\text{C}$ , and given an ambient air temperature between 9 and  $35^{\circ}\text{C}$ , is  $\pm 1^{\circ}\text{C}$ , or  $\pm 1\%$  of the reading. The camera offers a built-in emissivity-



correction option, which was not used for this study. Apart from the infrared pictures, the camera allowed us to take pictures in the visible spectrum simultaneously.

160 Where possible, pictures were processed semi-automatically as described in Resler et al. (2017). This processing required 4 well-defined points occurring at each picture, which were used to correct for changes in camera positioning between the measurements, as the camera was carried from one location to another. Pictures, which did not allow for semi-automatic processing (mostly ground images) were handled manually and temperatures were extracted by the FLIR Tools v5.13.18031.2002 software (<https://www.flir.com/products/flir-tools/>). Examples of semi-automatic and manually processed images are shown in  
165 Fig. S4.

Surface temperature measured by the FLIR SC660 was compared with the data from heat flux measurements at Sinkule house described in Sect. 2.3.2. The results are shown in Fig. S5. The IR camera generally gives higher values than the TRSYS01 system: in summer ground floor temperatures are on average 1°C higher (range of differences was between 0.0 and 2.8°C) and 1<sup>st</sup> floor on average 0.1°C higher (range of differences between -2.0 and +1.3°C). In winter the ground floor temperatures are  
170 on average 2.1°C higher (range of differences between 0.5 and 3.5°C) and 1<sup>st</sup> floor on average 1°C higher (range of differences between -0.6 and 2.0°C).

### 2.3.2 Wall heat fluxes measurement

Heat fluxes through the building facade and window were measured by the high-accuracy building thermal resistance measuring system TRSYS01 equipped with two HFP01 heat flux plates and two pairs of thermocouples (TC). Operating temperature range  
175 of HFP01 and TC is -30 to +70°C. Declared sensitivity of temperature difference measurements between inner and outer side of the wall is 0.02°C and heat flux measurement resolution 0.02 W.m<sup>-2</sup>. Calibration uncertainty of HFP01 is ±3 % (Hukseflux, 2020). Heat fluxes were measured through the north-east-facing wall of the Sinkule house and through the north-facing wall and window of the building in Zelená Street (Fig. 2). Position of the sensors on both buildings is shown in Fig. S6. Silicone glue was used to attach the sensors to the outside wall in the 1<sup>st</sup> floor of Sinkule house during the winter campaign. Otherwise  
180 sensors were mounted by a two-sided carpet tape.

The Sinkule house was built before World War II with walls made of construction blocks. The ground floor wall is 34 cm thick, without insulation and the facade is made of ceramic tiles. The wall in the 1<sup>st</sup> floor is 41 cm thick including 6 cm thick polystyrene insulation on the outer side. Facade surface is scratched plaster with scratches of 1–2 mm depth (see Fig. 2).

The house in Zelená Street is a typical representative of buildings in the area with walls made of bricks. Wall thickness at  
185 the place of measurement was approx. 30 cm with 2.5-cm lime-cement plaster on the inner and outer side of the wall. Heat flux measurement through the window was not used in PALM validation and therefore is not described here. A quality check measurement was done at the beginning of the summer campaign – sensors were placed side-by-side in the 1<sup>st</sup> floor of Sinkule house between 19 July 17:40 CEST and 20 July 12:00 CEST. Absolute difference of the facade surface temperature was 0.0–1.5°C with a median value of 0.1°C. Absolute difference of measured heat fluxes was 0.0–2.1 W.m<sup>-2</sup> with a median value of  
190 0.6 W.m<sup>-2</sup>.

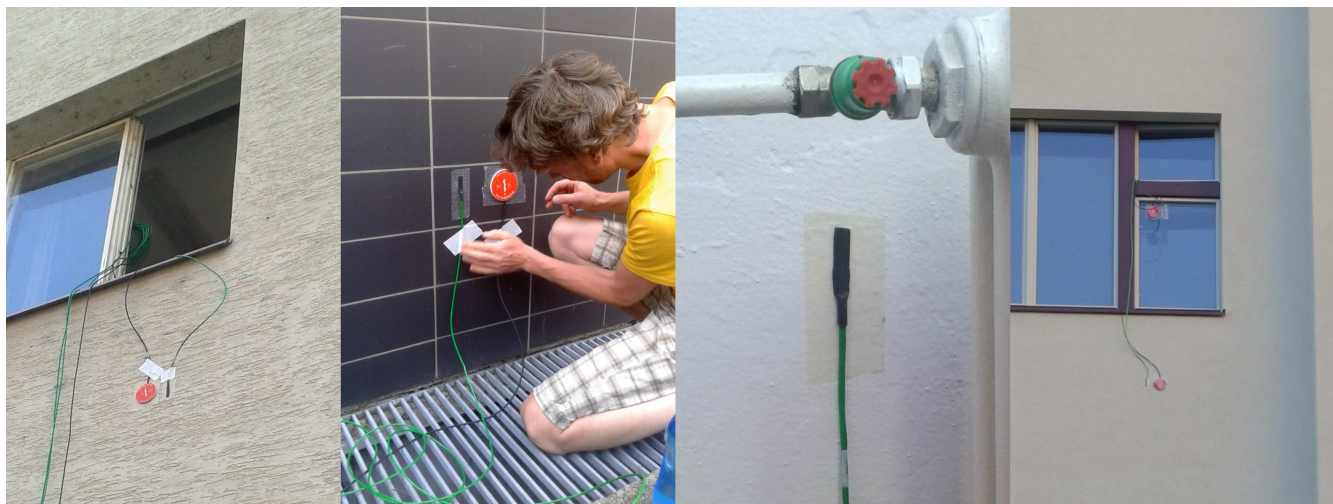


**Figure 2.** Detail of heat flux sensors and thermocouples mounting. Left - Sinkule house 1<sup>st</sup> floor; center-left - Sinkule house ground floor; center-right - Sinkule ground floor - inner temperature sensor; right - Zelená Street. For Sinkule house and Zelená Street location see Fig. 1.

### 2.3.3 Vehicle observations

Air quality and meteorological measurements in the street canyons were obtained by two monitoring vehicles, which were shuttled periodically among the three locations marked as green squares in Fig. 1. One location was in Jugoslávských partyzánů Street (Jug. p. St.), an approx. 42-m wide boulevard with sparse trees. The two remaining locations were in the 25-m wide Terronská Street next to the Bubeneč house and the Orlík house. Next to the Bubeneč house, there are full-grown broadleaf trees with crowns covering the whole street. Broadleaf trees next to the Orlík house are smaller and their crowns are covering  $\frac{2}{3}$  of the street canyon in maximum. Buildings in all locations are approx. 25 m high. Pictures of the measurement locations are shown in Fig. S7. The observations were organised in a way to provide information about air quality and meteorological conditions in the three locations but also to compare the east and west side of the street canyon. Each monitoring vehicle remained at a particular location for at least two whole days (see Table S2 and Table S3). Based on our own traffic census from 4–6 December 2018, the total workday load in Terronská St. (Bubeneč house) is 7,700 vehicles, which is approximately 44 % of the traffic intensities in Jug. p. St. The number of small trucks (60) in Terronská St. is only 20 % of their count in Jug. p. St. and the number of busses (20) is only 2 % of their count in Jug. p. St. There was only one large truck per day registered in Terronská St. compared to approx. 80 in Jug. p. St. Apart from the street canyon measurements, one stationary monitoring vehicle was located in the yard of the Sinkule house during the whole campaign to provide the urban background meteorological and air quality values.

The vehicles in the street canyons were equipped with analyzers of  $\text{NO}_x$ ,  $\text{NO}_2$ ,  $\text{NO}$ ,  $\text{O}_3$ ,  $\text{SO}_2$ ,  $\text{CO}$ ,  $\text{PM}_{10}$ ,  $\text{PM}_{2.5}$ , and  $\text{PM}_1$  measured at the top of the vehicle roof (approx. 4.6 m). Calibrations of all air quality analyzers were performed during the transfer between the locations to eliminate loss of data during parallel measurements. Meteorological variables measured



210 included wind speed and direction and turbulent flow characteristics measured by the METEK 3D ultrasonic anemometer on  
a meteorological mast at a height of about 6.8 m above the ground (to reach above tree crowns), air temperature, relative  
humidity, global radiation and atmospheric pressure. One-minute averages of all entities were available from the instruments.  
For further analysis and PALM evaluation, 10-minute averages of measured variables were used. Both vehicles also had a video  
camera placed at the front windscreen. The recording was then used for detailed time disaggregation of traffic emissions in the  
215 measured location and for calibration of an automatic counting system (see Sect. 3.4).

The vehicle in the yard of the Sinkule house was measuring the same variables with the same time resolution except for  
the following differences: PM1 was not measured; wind speed and direction were measured by the GILL 2D WindSonic  
anemometer at the standard height of 10 m.

### 2.3.4 Mobile measurements

220 On selected days of the measurement campaigns, mobile measurements using a dedicated monitoring vehicle were performed  
to get more detailed information on air quality in the inner domain (12, 18, 19 July, 26 November, and 4 December). The vehicle  
was moving between the locations shown on Fig. 1, stopping and measuring in each of them for five minutes. Two loops were  
made on every measurement day. On 19 July only one loop among locations 3, 6, 15–17 was made, but the measurements  
took 15–20 min. The vehicle was equipped with NO<sub>x</sub>, NO<sub>2</sub>, NO, O<sub>3</sub>, SO<sub>2</sub>, CO, PM<sub>10</sub>, PM<sub>2.5</sub>, and PM<sub>1</sub> analyzers. A Garni 835  
225 weather station was used for an indicative measurement of temperature, wind and relative humidity starting from the second  
measurement on 17 July 2018. Some measurements were not available on particular days – details are given in Table S2 and  
Table S3.

### 2.3.5 Higher level observations

To get information about higher levels, two additional observations were proposed in the scope of the observation campaign.  
230 The first one was a stationary measurement of wind flow above rooftops in the area of interest throughout the campaign  
duration. A 2D anemometer was installed on the roof of the Faculty of Civil Engineering of the Czech Technical University  
– the highest building in the inner domain (approx. 60 m high) (FSv; see Fig. 1). Measurement frequency was 1 second. The  
10-minute averages were used for further evaluation. The second one was a measurement of vertical profiles in the lowest part  
of the atmosphere. Originally, two one-day drone observation campaigns were scheduled. Due to administrative restrictions,  
235 the summer drone observations were not realised and the winter part had to be moved from the center of inner domain to  
the location marked in the Fig. 1. Also, the maximum flight altitude had to be limited to 80 m above ground. The drone was  
equipped with the GRIMM Portable Laser Aerosol spectrometer and Dust Monitor Model 1.108 and HC2A-S probe from  
ROTRONIC for the measurement of temperature and relative humidity (ROTRONIC, 2020). Unfortunately, the probe showed  
a longer than expected relaxation time and was not able to adapt quickly enough during the descent. Recalculation of particle  
240 counts to mass concentration was also burdened with large errors. The obtained results were not reliable enough to be included  
in PALM validation, but temperature and relative humidity profiles are provided in supplements (Fig. S8 and Fig. S9).



### 2.3.6 Standard CHMI observations used for validation

The following standard meteorological and air quality measurements were used for the evaluation of WRF and CAMx simulations (which provided initial and boundary conditions for PALM; see Sect. 3.3). This evaluation is presented in Sect. 4.1.

245 WRF vertical profiles were evaluated against the upper air soundings from Praha-Libuš (WMO ID 11520) station located in the south suburb of Prague, 11 km apart from the center of PALM inner domain. Radiosonde is released every day at 0, 6, and 12 UTC. For the evaluation of global radiation, two meteorological stations were selected: the already mentioned Praha-Libuš station and Praha-Karlov station situated in a densely built-up area in the wider center of Prague approximately 4 km from the PALM inner domain. PM<sub>10</sub> and NO<sub>x</sub> concentrations provided by the CAMx model were compared with the measurement from

250 automated air quality monitoring stations. Only 5 background stations closest to the PALM inner domain were used. Station locations are shown in Fig. S10. More detailed information about stations is given in Table S4 and Table S5.

## 3 Model simulation setup

### 3.1 PALM model and domains configuration

PALM model system version 6.0 revision 4508 (Maronga et al., 2015, 2020) was utilized for this validation study. It consists

255 of the PALM model core and embedded modules and of PALM-4U components which have been specifically developed for modelling urban environments. The PALM model core solves the incompressible, filtered, Boussinesq-approximated Navier-Stokes equations for wind ( $u$ ,  $v$ ,  $w$ ) and scalar quantities (potential temperature, water vapor mixing ratio, passive scalar) on a staggered Cartesian grid. The sub-grid scale terms that arise from filtering are parametrized using a 1.5-closure by Deardorff (1980) with modifications after Moeng and Wyngaard (1988) and Saiki et al. (2000). Buildings and orography are mapped onto

260 the Cartesian grid using the mask method (Briscolini and Santangelo, 1989), where a grid cell is either 100% fluid or 100% obstacle. The advection terms are discretized by a 5<sup>th</sup> according to Wicker and Skamarock (2002). For temporal discretization, a 3<sup>rd</sup>-order low-storage Runge-Kutta scheme (Williamson, 1980) is applied. The Poisson equation is solved by using a multigrid scheme (Maronga et al., 2015).

The following urban canopy related PALM and PALM-4U modules were employed in this study: the land surface model

265 (LSM, Gehrke et al., 2020; to be submitted to GMD) was utilized to solve the energy balance over pavements, water- and other natural-like surfaces, the building surface model (BSM, formerly USM, see Resler et al., 2017) was used to solve the energy balance of building surfaces (walls and roofs). The BSM was configured to utilize an integrated support for modelling of fractional surfaces (Maronga et al., 2020). Dynamic and thermodynamic processes caused by resolved trees and shrubs were managed by the embedded plant-canopy model (PCM). Radiation interaction between resolved scale vegetation, land-surface,

270 and building surfaces was modelled via the radiative transfer model (RTM, Krč et al., 2020; to be submitted to GMD). Downwelling shortwave and longwave radiation from the upper parts of the atmosphere, which were used as boundary conditions for the RTM, were explicitly prescribed from stand-alone Weather Research and Forecasting model (WRF; see Sect. 3.3 for details) simulation output for the respective days rather than modelled by e.g. the Rapid Radiation Transfer Model for Global



Models (RRTMG). This way, effects of mid- and high-altitude clouds on the radiation balance were considered in the simula-  
275 tions. It is needed to note that without applying the RRTMG some physical processes such as vertical divergence of radiation  
fluxes leading to heating / cooling of the air column itself were missed, which may become especially important at nighttime.  
However, sensitivity tests with RRTMG applied revealed that the effect on nighttime air temperature was negligible in our  
simulations. In addition to the meteorological component, the embedded online chemistry model (Khan et al., 2020; to be  
submitted to GMD) was applied to model concentrations of  $\text{NO}_x$ ,  $\text{PM}_{10}$ , and  $\text{PM}_{2.5}$ . Chemical reactions were omitted in this  
280 case to simulate purely passive transport of the pollutants. For a human thermal comfort estimation the PALM biometeo-  
rological module (Fröhlich and Matzarakis, 2019) was used. However, campaigns were not designed for their evaluation and  
these results were not validated.

Additionally both self- and online nesting features of PALM-4U were utilised. Self-nesting means that a domain with a  
finer resolution can be defined inside a larger domain and this subdomain (child domain) receives its boundary conditions  
285 from the coarse-resolution parent domain at every model timestep. Here, a one-way nesting without any feedback of the child  
simulation on the parent simulation (Hellsten et al., 2020; to be submitted to GMD) was applied. The coarse-resolution parent  
simulation itself received its initial as well as lateral and top boundary conditions from the simulations of the mesoscale model  
WRF transformed to a PALM dynamic driver (see Sect. 3.3). The boundary values were updated at every model time step, and  
this process is hereafter referred to as offline nesting (Kadasch et al., 2020; to be submitted to GMD). As the offline nesting  
290 was used for coupling to the mesoscale model that does not resolve turbulence, the turbulence was triggered at the model  
boundaries using an embedded synthetic turbulence generator (STG) according to Xie and Castro (2008), which imposed  
spatially and temporally correlated perturbations every time-step onto the velocity components at the lateral boundaries. The  
initial and boundary concentrations of modelled pollutants of the parent domain were taken from simulations of the CAMx  
model (Comprehensive Air-quality Model with Extensions; see Sect. 3.3). For more detailed information about the PALM  
295 model, embedded modules and the PALM-4U components see Maronga et al. (2020) and the companion papers in this special  
issue.

The location of the parent and child modelling domains is shown by Fig. S1. The parent domain extends horizontally by  
 $4 \times 4 \text{ km}^2$  in the x- and y-direction, respectively, with an isotropic grid spacing of 10 m. The vertical z-direction is covered by  
162 layers for summer and 82 layers for winter simulations, respectively. The vertical grid spacing is 10 m for the lower 250 m  
300 of the domain, well above the building-affected layer the vertical grid was successively stretched up to a maximum vertical grid  
spacing of 20 m in order to save computational resources. The domain top is at 2,930 m for summer and 1,330 m for winter  
simulations, respectively. This extent safely covers the convective layer with a sufficient buffer. The child domain extends by  
 $1,440 \times 1,440 \times 242 \text{ m}^3$  in the x-, y-, and z-direction, respectively, with an isotropic grid spacing of 2 m.

Parent and child domains were initialized by vertical profiles of u, v, w, potential temperature and mixing ratio, soil moisture  
305 and soil temperature, transformed from WRF simulations (see Sect. 3.3). Since the initial soil and wall temperatures from a  
mesoscale model are only a rough estimate due to its aggregated nature, the PALM spin-up mechanism was applied (Maronga  
et al., 2020). During a 2-day spinup, the atmospheric code was switched-off and only the LSM and BSM together with the



radiation and RTM model were executed. By this, the material temperatures were already closer to their equilibrium value and significant changes in material temperatures at the beginning of the simulation were avoided.

### 310 3.2 Urban canopy properties

Data availability, their harmonization and costs/efficiency trade-offs often needs to be considered (Masson et al., 2020). For solving the energy balance equations as well as for radiation interactions, BSM, LSM, and RTM require using detailed and precise input parameters describing the surface materials (e.g., albedo, emissivity, roughness length, thermal conductivity, thermal capacity, capacity and thermal conductivity of the skin layer). Also plant canopy (trees and shrubs) is important as it affects the flow dynamics, heating and evapotranspiration as well as the radiative transfer within the urban environment. Urban and land surfaces and sub-surface materials become very heterogeneous in a real urban environment when going to very fine spatial resolution. Any bulk parameterization for the whole domain setting would therefore be inadequate. Instead, a detailed setting of these parameters was supplied everywhere possible. To obtain needed detailed data, a supplemental on-site data collection campaign was carried out and a detailed database of geospatial data was created. Land-cover data are based on a combination of national (ZABAGED) and city of Prague (Prague OpenData) databases. ZABAGED geodatabase (ČÚZK, 2020) distinguishes 128 categories of well-targeted geographical objects and fields (e.g. built-up areas, communications, hydrology, vegetation, and surface). Prague OpenData geodatabase (Prague Geoportal, 2020) distinguishes many local, user-specified, GIS layers, e.g. plans with actual and future development, land-cover for architects, photogrammetry-based digital elevation model (DEM) etc. Building heights were available from the Prague 3D model, maintained by the Prague Institute of Planning and Development. For the first tree canopy data mapping, LiDAR scanning was used in combination with photogrammetric-based DEM. Derived heights were manually calibrated using terrain mapping campaign and extended with additional parameters (e.g., crown height, width and shape, trunk height and width). All descriptions of surfaces and materials and their properties were collected in GIS formats and then preprocessed into the PALM NetCDF input file corresponding to the PALM Input Data Standard (PIDS; Heldens et al., 2020). This file includes information on wall, ground, and roof materials and properties similar to that used to estimate surface and material properties in Resler et al. (2017) and Belda et al. (2020).

Each surface is described by material category, albedo, and emissivity, BSM surfaces additionally carry thickness, and window fraction. Parameters, such as thermal conductivity and capacity, are assigned to categories estimated based on surface and storage material composition. In case of walls and roofs, which are limited to four layers in the current version of BSM, this means the parameters of the two outer layers were assigned according to the properties of the covering material (e.g. plaster or insulation) while remaining layers were initialized by properties of the wall material (e.g. bricks, construction blocks, concrete, insulation). Wall and roof properties are described in table located in Table S6. In case of pavements and other LSM surfaces, all parameters except albedo and emissivity were assigned according to the PALM LSM categories.

Each tree in the child domain was described by its position, diameter, trunk parameters and vertically stratified base leaf area density. The actual distribution of the leaf area density (LAD) within the treetop was then calculated according to the available light exposure of the particular gridbox inside the treetop according to the Beer-Lambert law, leading to lower LAD in the centres of large and/or dense treetops. Note, at the moment PALM does not consider the effect of trunks on the dynamic flow



field and the thermodynamics, only LAD is considered. However, for the winter case leafless deciduous trees were considered by 10 % of their summer LAD to account for the effect of trunks and branches on the flow field.

### 3.3 Initial and boundary conditions

345 Initial and boundary meteorological conditions for the parent domain of the PALM simulations were obtained from the WRF model (Skamarock et al., 2008), version 4.0.3. The WRF model was run on three nested domains with horizontal resolutions of 9 km, 3 km and 1 km and 49 vertical levels. The inner domain has  $84 \times 84$  grid points in the horizontal. The configuration was standard but parameterizations have been chosen so as to decrease possible discrepancies which might arise from boundary conditions. NOAH LSM (Chen and Dudhia, 2001) and RRTMG radiation (Iacono et al., 2008) have been used in  
350 all simulations. As for PBL parameterization, Yonsei University scheme (Hong et al., 2006) has been chosen for the summer episodes while for the winter episodes Boulac urban PBL (Bougeault and Lacarrère, 1989) scheme has been used. Except for that, no other urban parameterization has been used in the WRF model. MODIS land use categories have not been altered. The WRF output data have been collected from overlapping runs of length 12 hours, initialized from the GFS operational analyses and predictions. The first six hours of each run served as a spin-up. The boundary conditions for the offline nesting have been  
355 generated from forecast horizons 7–12.

Air quality simulations that served as chemical initial and boundary conditions were conducted using the chemistry transport model (CTM) CAMx version 6.50 (ENVIRON, 2018). CAMx is an Eulerian photochemical CTM that contains multiple gas phase chemistry options (CB5, CB6, SAPRC07TC). Here, the CB5 scheme (Yarwood et al., 2005) was invoked. Particle matter was treated using a static two-mode approach. Dry deposition was calculated following Zhang et al. (2003) and for wet  
360 deposition, the Seinfeld and Pandis (1998) method was used. To calculate the composition and phase state of the ammonia-sulfate-nitrate-chloride-sodium-water inorganic aerosol system in equilibrium with gas phase precursors, the ISORROPIA thermodynamic equilibrium model was used (Nenes et al., 1998). Finally, secondary organic aerosol (SOA) chemistry was solved using the semi-volatile equilibrium scheme SOAP (Strader et al., 1999).

CAMx was coupled offline to WRF meaning that CAMx ran upon WRF meteorological outputs. WRF outputs were then  
365 translated to CAMx input fields using the WRFCAMx preprocessor provided along with the CAMx source code (see <http://www.camx.com/download/support-software.aspx>). For those CAMx input variables that were not available directly in WRF output, diagnostic methods were applied. One of the most important inputs for CAMx that drives the vertical transport of pollutants, is the coefficient of vertical turbulent diffusion ( $K_v$ ).  $K_v$  is a significant parameter that determines the city scale air pollution and it is substantially perturbed by the urban canopy effects (Huszar et al., 2018a, b, 2020). Here, the “CMAQ”  
370 scheme (Byun, 1999) was applied for  $K_v$  calculations.

WRF and CAMx outputs were then postprocessed to the PALM dynamic and chemistry driver. The data were transformed between coordinate systems and a horizontal and vertical interpolation was applied. As the coarse-resolution model terrain would not match the PALM model terrain exactly, the vertical interpolation method included terrain matching and the atmospheric column above the terrain was gradually stretched following the WRF hybrid vertical levels as they were converted to



375 the fixed vertical coordinates of the PALM model. The interpolated airflow was adjusted to enforce the mass conservation. Detailed technical description of the 3D data conversion procedure is beyond the scope of this study.

Emission data for Prague used in the CAMx model were the same as described in the next chapter. Other emission inputs are described in detail in Ďoubalová et al. (2020).

### 3.4 Emission data

380 Air pollution sources for our particular case are dominated by the local road traffic. Annual emissions totals were based on the traffic census 2016 conducted by the Technical Administration of Roads of the City of Prague – Department of Transportation Engineering (TSK-ÚDI). Emissions itself were prepared by ATEM (Studio of ecological models; <http://www.atem.cz>) using MEFA 13 model. Jugoslávských partyzánů and Terronská Street, where air quality was measured during the campaigns, were covered by this census. Emissions from streets not included in the census were available in a grid with 500m spatial resolution.

385 These emissions were distributed between the streets not covered by the census according to their parameters. Particulate matter (PM) emissions included resuspension of dust from the road surface (Fig. 3). Time disaggregation was calculated using a Prague transportation yearbook (TSK-ÚDI, 2018), public bus timetables, and our own short-time census (19–21 July and 4–6 December). This time disaggregation was the same for the primary emissions (exhaust, brake wear etc.) as well as for resuspended dust. Higher dust resuspension caused by sprinkle material during winter time was not considered.

390 Traffic data were supplemented by emissions from stationary sources from the Czech national inventory REZZO: point sources correspond to the year 2017 (the latest year available at the time of model input preparation). Residential heating was based on 2017 inventory and rescaled to 2018 multiplying by the ratio of degree days  $DD(2018)/DD(2017)$ ;  $DD(r)$  is the sum of the differences between the reference indoor temperature and the average daily outdoor temperature on heating days. Residential heating emissions were available on elemental dwelling units - urban areas with average area 0.5 km<sup>2</sup>, and were

395 spatially distributed to building addresses, where local heating source is registered, proportionally to the number of flats. Time disaggregation of point source emissions was based on monthly, day-of-week and hour-of-day factors (Bultjes et al., 2003; available also in Denier van der Gon et al., 2011). Residential heating emissions were distributed to days according to the standardized load profile of natural gas supply for the households, which use it for heating only (Novák et al., 2019; OTE, 2020). Daily variation of residential heating emissions was taken from Bultjes et al. (2003).

400 All these input emission data were processed into the PALM input NetCDF files corresponding to the PALM Input Data Standard (PIDS).

### 3.5 Observation operator

To compare modelled and observed values, an observation operator which links model variables to observed quantities is needed. In case of vehicle measurements, the situation was straightforward; horizontally, we used atmospheric quantities and

405 chemical compounds at the grid cell closest to the real placement of the sensors while vertically, we performed linear interpolation to the real height of the sensor. This approach was sufficient given the fine 2m resolution within the child domain. In case of surface observations at grid-aligned surfaces (walls parts without step-like structures), the modelled values at the

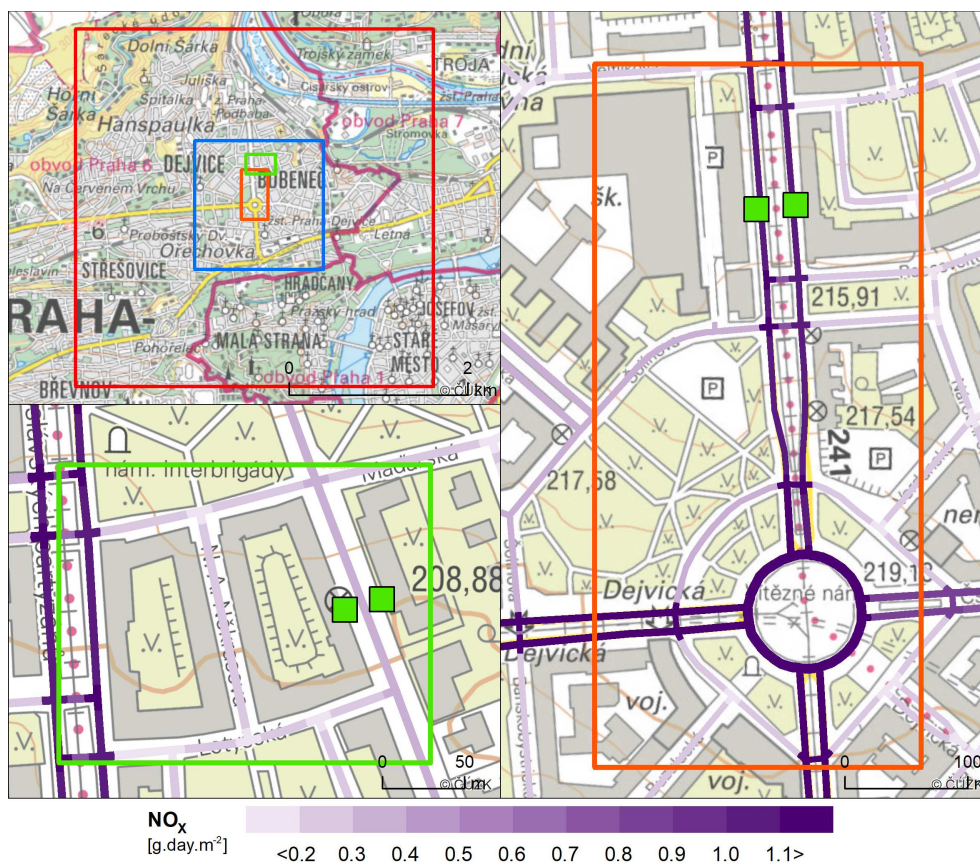


**Figure 3.** Nitrogen oxides ( $\text{NO}_x$ ) emitted by the cars along their trajectories in selected locations in Prague-Dejvice. Concentrations were summarized in  $\text{g}\cdot\text{day}^{-1}\cdot\text{m}^2$  and disaggregated to 1-hour time steps. Green squares represent air-quality locations in Terronská St., Bubeneč house (left bottom) and Jugoslávských partyzánů St. (right). The base map of the Czech Republic at 1:10,000 for the city of Prague was provided by Czech Office for Surveying, Mapping and Cadastre (ČÚZK, 2020).

nearest grid face according to the real placement of the sensor or evaluation point were also taken. However, at non grid-aligned walls, i.e. walls which are oriented in one of the south-west, south-east, north-west, and north-east directions, walls are approximated by step-like structures and choosing the nearest grid face is not unique any more as illustrated in Fig. 4. In this case, the orientation of the real wall cannot be sufficiently represented by the one grid face but is approximated by grid faces with perpendicular orientation. Hence, we virtually sampled surface quantities at both surfaces and calculated the modelling counterpart of the observation as the average of these values. In the following, the sampled values are plotted with suffixes “\_l” and “\_r” to distinguish between “left” and “right” adjacent faces and their average as the modelled value. Implications for the model evaluation as well as for the comparability of the model to the observations accompanied with the grid discretization are discussed in Sect. 4.3.5.



**Figure 4.** Illustration of mapping of a surface observation point on a wall into two grid faces.

## 4 Results

### 4.1 Evaluation of the driving synoptic-scale simulation

#### 4.1.1 Meteorology

420 Since the boundary conditions for the PALM simulations come from a model simulation, we need to check for potential  
misrepresentation of the real weather. First we assess the overall performance of the WRF model simulation on the synoptic  
scale by comparing the results with the known state of the atmosphere represented here by the ERA-Interim reanalysis and  
atmospheric soundings obtained by the CHMI weather balloons (downloaded from the University of Wyoming database;  
<http://weather.uwyo.edu/upperair/sounding.html>). Fig. 5 show maps of geopotential height at 500 hPa and 850 hPa comparing  
425 the results of the WRF simulation (9km domain) with the ERA-Interim reanalysis. The rest of the maps is in supplementary  
files; see Fig. S11 and Fig. S12.

Generally, the WRF simulations, being driven by the GFS, correspond very well to the ERA-Interim reanalysis in terms  
of 500 hPa geopotential height field with some shifts of the pressure field eastward on 19 July and northward on 21 July.  
Geopotential height at 850 hPa is also very well represented with some added detail mainly during the day of the summer  
430 month due to a better resolved topography in the higher-resolution regional model simulation.

Next, we evaluated the WRF results with atmospheric soundings for the station closest to our domain of interest, Praha-  
Libuš (note: the weather balloon measurements are taken only three times per day at 00, 06 and 12 UTC). Fig. 6 shows the  
vertical profile of potential temperature for 20–21 July and Fig. 7 for 4–5 December (vertical profiles for the rest of the episodes  
are included in the supplement; see Fig. S13, Fig. S14 and Fig. S15). Modelled profiles generally correspond well with the  
435 measurements with some notable exceptions in the surface layer (which is of the highest importance for this study, as the  
boundary conditions for the PALM simulations are taken from the lower levels) where the model tends to show a lower diurnal  
range underestimating stability in the night time and instability during the day.

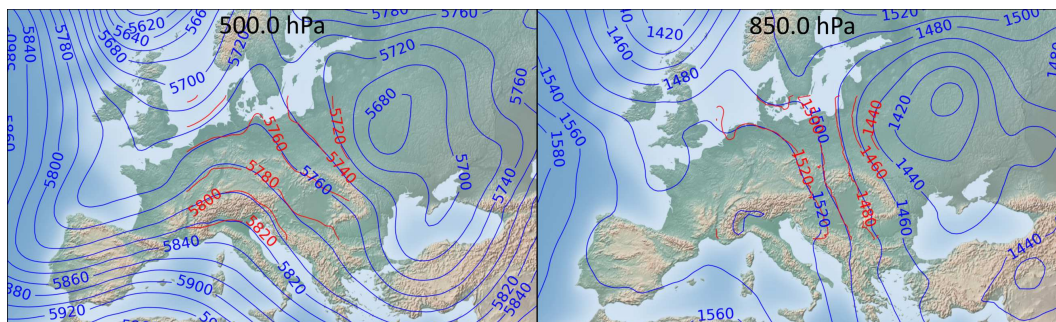


**Figure 5.** Geopotential height at 500 hPa (left) and 850 hPa (right) for 20 July 2018 00:00 UTC. Blue line is ERA-Interim reanalysis, red line is WRF simulation of 9-km domain. Background layer uses the public domain shaded relief map from Shaded Relief (2020).

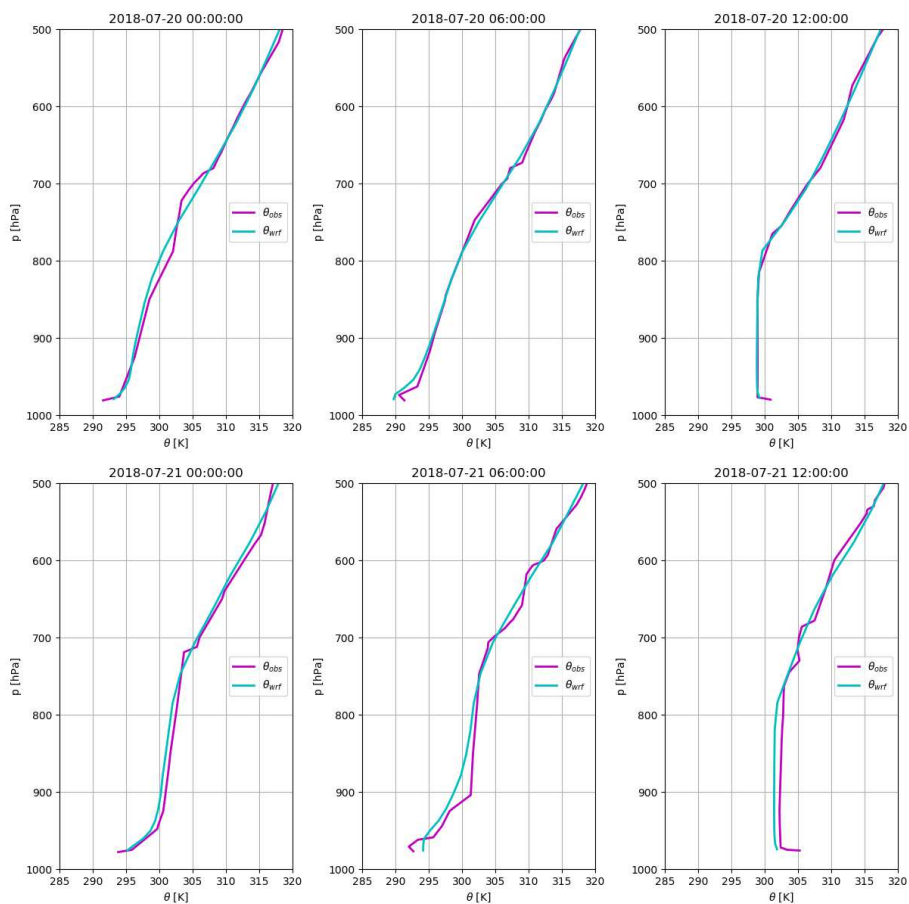


**Figure 6.** Vertical profile of potential temperature from the soundings balloon observations at the Praha-Libuš station (magenta) and the nearest grid box of the WRF simulation 1km domain (cyan) for 20–21 July.

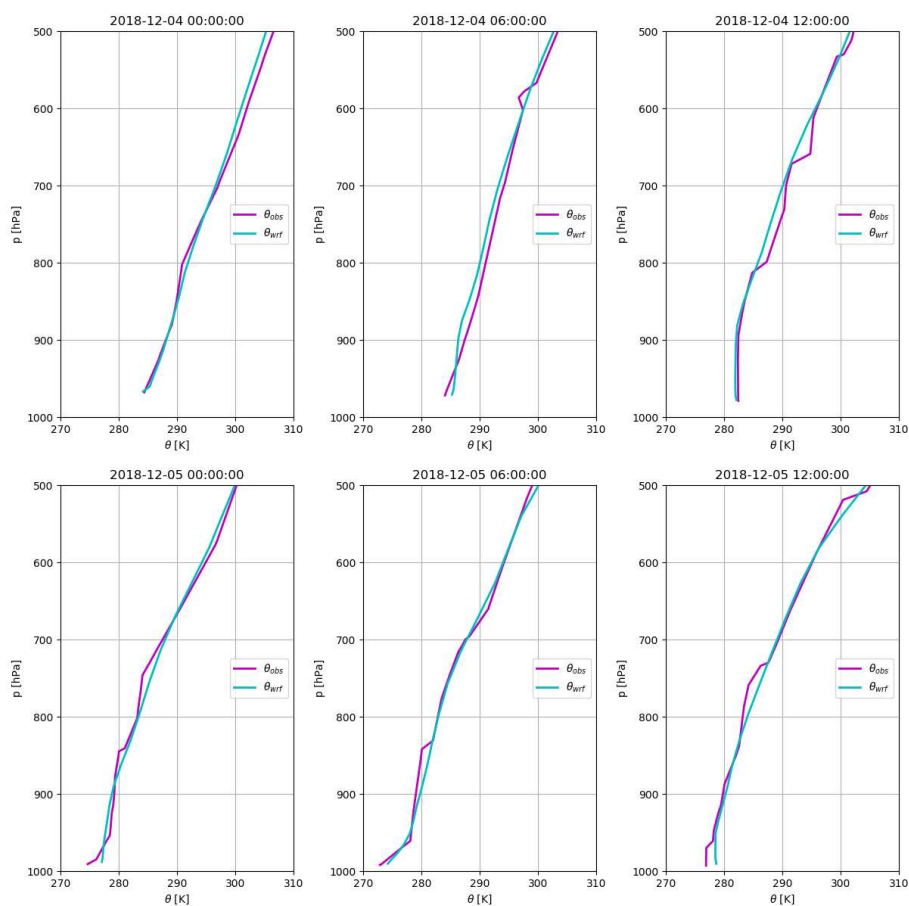


**Figure 7.** Vertical profile of potential temperature from the soundings balloon observations at the Praha-Libuš station (magenta) and the nearest grid box of the WRF simulation 1km domain (cyan) for 4–5 December.

Here we note that in case the boundary-layer depth is within the range of the horizontal grid resolution, which is especially the case for the summer simulations, Ching et al. (2014) and Zhou et al. (2014) showed that resolved scale convection can develop which depends on the horizontal grid resolution as well as on the applied boundary-layer scheme. For a nested LES into a mesoscale WRF simulation, Mazzaro et al. (2017) showed that such under-resolved convection may propagate into the LES domain biasing the location of the up- and downdrafts. In order not to bias our simulation results by under-resolved convection in WRF propagating into the LES, we checked the WRF-simulation output for the occurrence of under-resolved convection but did not find any (not shown).

In our setup, PALM simulations need radiation values from the WRF simulations as one of boundary conditions. To check for potential errors in these boundary conditions, we compare (see Fig. 8) global radiation as simulated by WRF (innermost 1km domain; black dots) in the grid box centered over the area of interest with observations at two CHMI stations in Prague with continuous global radiation measurements: Praha-Karlov (approx. 4 km southeast from the modelled area) and Praha-



Libuš (approx. 11 km south-southeast from the modelled area). WRF simulations show good agreement with observations  
450 in the summer campaign with some overestimation of the global radiation on 14 and 23 July at noon, most likely due to  
underestimation of cloud cover in the WRF simulation. During the winter campaign, the global radiation in WRF agrees with  
the observation at nighttime as well as during the morning and afternoon hours. However, WRF significantly overestimates the  
global radiation at noon due to underestimated cloud cover during this period of time.

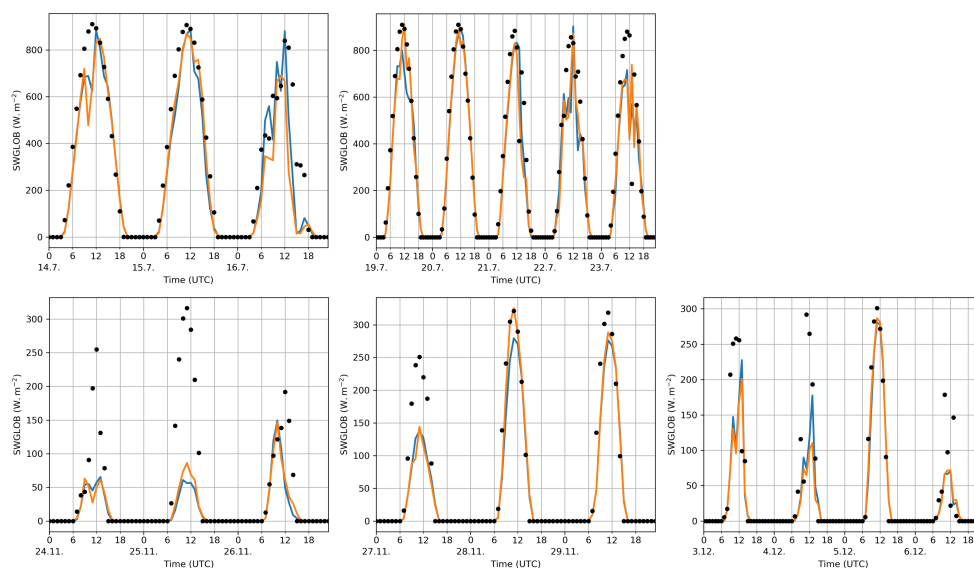


**Figure 8.** WRF modelled and observed global radiation for modelling episodes summer e1, e2 (top row) and winter e1, e2, e3 (bottom row) from CHMI stations Praha-Karlov (blue), Praha-Libuš (orange); WRF simulation (black).

#### 4.1.2 Air quality

455 For the CAMx model validation, urban background air quality monitoring stations closest to the PALM outer domain were  
used (see Sect. 2.3.6). Validation was performed for hourly average concentrations of  $\text{NO}_x$  and  $\text{PM}_{10}$ . Only PALM episodes  
were included (i.e. 14–15 and 19–23 July for summer and 24–29 November and 4–6 December for winter). Metrics according  
to Britter and Schatzmann (2007) and Chang and Hanna (2004) for both campaigns are summarized in Table 1 (note that  
fractional bias values are positive, when model underpredicts observations). R statistical software (R Core Team, 2019) and  
460 openair package (Carslaw and Ropkins, 2012) was used.

For  $\text{NO}_x$ , the metrics show a significant underprediction of the measured concentrations (FB ca. 0.8) for both summer and  
winter episodes. Nevertheless, the daily variation is captured quite well (see Fig. S16) although in winter modelled peaks  
in the evening are larger than in the morning, while in the observed data it is just opposite. Analysis of PALM simulated  
concentrations in section 4.6 will show that this bias is not present there.



**Table 1.** Evaluation of CAMx 1-h concentrations against urban background stations.

	NO <sub>x</sub>	NO <sub>x</sub>	PM <sub>10</sub>	PM <sub>10</sub>
	Summer	Winter	Summer	Winter
N	684	816	907	1078
mean obs [ $\mu\text{g}\cdot\text{m}^{-3}$ ]	22.6	59.5	22.1	30.4
mean mod [ $\mu\text{g}\cdot\text{m}^{-3}$ ]	10.1	24.4	13.4	33.3
FB	0.76	0.84	0.49	-0.09
NMSE	1.51	2.15	0.65	0.53
FAC2	0.38	0.31	0.50	0.69
R	0.54	0.28	0.34	0.13

N is the number of valid data pairs. Apart from means of observed and modelled values, metrics from Britter and Schatzmann (2007) are given: FB - fractional bias (note that FB>0, when model underpredicts observations), NMSE - normalized mean square error, FAC2 - fraction of predictions within a factor of two of the observations, R - Pearson correlation coefficient.

465 Summer PM<sub>10</sub> concentrations are less underestimated (FB ca. 0.5) and morning and evening peak is more sharp and appears  
 ca. 1 h earlier than in observations. Winter PM<sub>10</sub> are even a bit overestimated but CAMx model is not able to represent their real  
 daily variation. Modelled daily variation is very similar to that for NO<sub>x</sub>, which indicates that it is dominated by daily variation  
 of traffic, while in reality different sources play more important role.

#### 4.2 PALM simulation characteristics, vertical profiles

470 In order to check whether the observed boundary-layer structure is represented realistically by the LES simulation, we com-  
 pare model results against radio-soundings from the Praha-Libuš station. Please note, the meteorological station is positioned  
 roughly 11 km south-southeast from our area of interest and in an area with different topography and urban topology located  
 on the southern edge of the city, which means that the comparison with model simulation is not exact and especially within the  
 lower parts of the boundary layer modelled and observed profiles need not necessarily match due to the different surroundings.

475 Figure 9 shows vertical profiles of potential temperature and wind speed from PALM together with the soundings for the  
 summer e2 case. Taking into account the limitations of this comparison, model simulations show good agreement with obser-  
 vations capturing the overall shape of the profile with a slight tendency of underestimation of the actual values in the summer  
 episode. However, in the lower layers the model tends to underestimate the diurnal variations showing lower stability during  
 the night and lower instability during the day.

480 During the first night (Fig. 9) the modelled and observed temperature profiles agree well near the surface, while further above  
 the modelled profiles show slightly smaller values, although the shape of the profiles is similar to the observed one. The wind  
 speed in the residual layer is much smaller than in the measured profile and remains approximately constant until noon while  
 the measured wind slows down and becomes closer to the simulation during the day. On the following day, the modelled and  
 observed temperature profiles agree fairly well up to 1,500 m, both indicating a vertically well mixed boundary layer. At that  
 485 point in time the modelled profile indicates a higher boundary-layer top at about 1,950 m, while the observed profile indicates a

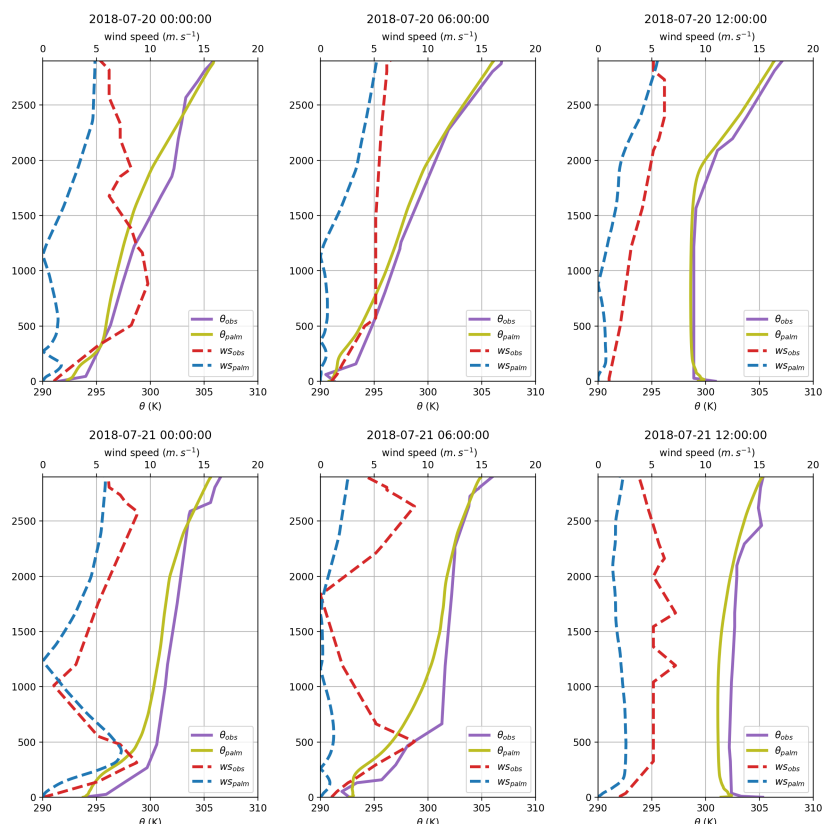


**Figure 9.** Vertical profile of potential temperature (solid line) and wind speed (dashed line) for the summer e2 episode from the weather balloon soundings at Praha-Libuš station (purple and red) and parent domain average from the PALM model simulation (yellow and blue).

boundary-layer top at about 1,550 m. However, as already mentioned above, these discrepancies can also be due to the different location rather than a misrepresentation of the model, where the boundary-layer depth over the more strongly heated built-up area may be deeper than over suburban areas (Brugger et al., 2018). During the second night, the modelled profile indicates a cooler boundary layer which is less stable near the surface. On 21 July at 00:00, the wind speed profile agrees well with the measurement. However, at 06:00 the low-level jet is missing in the simulation. On the following day, again the modelled and the observed temperature profiles agree, although the modelled boundary layer tends to be cooler by about 1 K. The wind speed is almost constant and uniformly smaller than the observations.

Figure 10 shows the modelled and observed profiles of potential temperature and wind speed during the winter e3 episode. During the first night the temperature profile suggests a more pronounced stable boundary layer. On the following day the modelled temperature profile agrees fairly well with the observed profile. However, the shape of the wind speed profile differs from the measured one. Notably, the boundary-layer values differ considerably. On the second night and the following second



day the temperature profiles agree, even though the modelled profile indicates a slightly warmer near-surface layer by about 1 K compared to the observed profile.

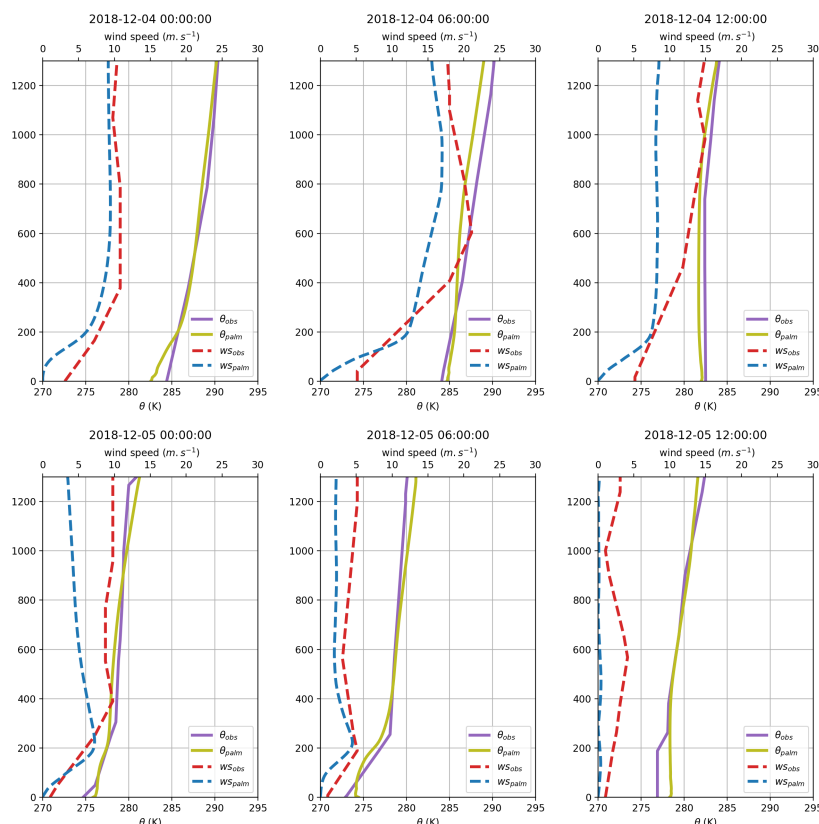


**Figure 10.** Vertical profile of potential temperature (solid line) and wind speed (dashed line) for the winter e3 episode from the weather balloon soundings at Praha-Libuš station (purple and red) and parent domain average from the PALM model simulation (yellow and blue).

Figure 11 presents the time series of the wind speed and wind direction at the roof of the highest building of the inner LES domain (FSv - Faculty of Civil Engineering CTU). The average wind speed in PALM agrees with the observations. In the summer e2 episode the agreement is very good. The disagreement in the vertical profile at midnight of 20 July might be explained by the difference of timing of the sharp wind speed decrease as suggested by the FSv time series. Also in the morning of 21 July when the vertical profiles show significant disagreement in higher levels the difference at FSv is much smaller. There is one extraneous sharp peak of wind speed in the afternoon of 21 July in the PALM results. 22 July is simulated very well including the morning and evening secondary maxima. The wind direction changes on 19 and 22 July are captured well with some disagreement in the timing.

In the winter e3 episode the difference is larger. The morning of 4 December shows disagreement in the wind direction followed by a sharp extraneous peak in wind speed. After a well-predicted decrease in the morning of 5 December the wind

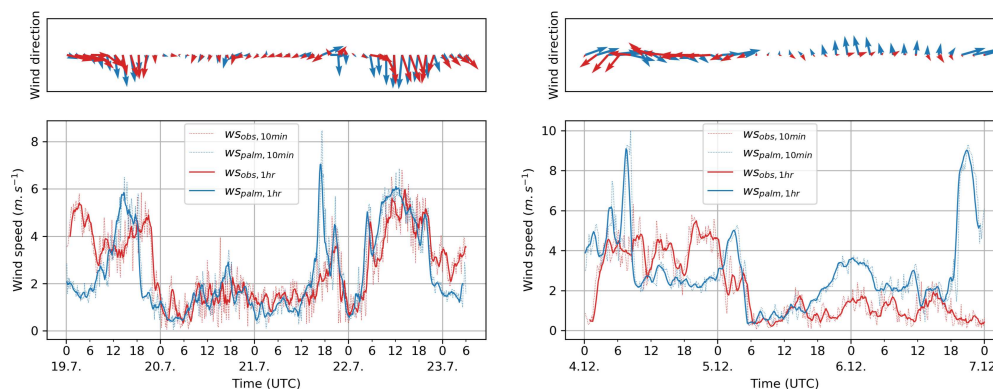


**Figure 11.** Time series of wind speed and wind direction at the roof of the tall building of the Faculty of Civil Engineering of the Czech Technical University for summer episode e2 and winter episode e3. Thin lines represent 10-minute averages and the thick lines 1-hour moving averages of wind speed. The arrows represent 2-hour averages of wind direction.

speed somewhat overpredicted and there is another large extraneous peak in the evening of 6 December. However, the wind direction does not agree. This confirms the disagreement of the wind profiles in Fig. 10. The time series of the wind speed and wind direction for episodes summer e1, winter e1, and e2 are presented in supplements in Fig. S17.

### 4.3 Surface temperature

Figure 12 shows an example of a 3D view of instantaneous surface temperature in the child domain on 20 July 2018 at 14:00 CET. The heterogeneous distribution of surface temperature reflects the distribution of pavements and green areas, with higher temperatures over paved areas and at building walls and roofs. Below the trees, where most of the shortwave radiation is absorbed within tree crowns, surface temperatures about 290 K are modelled (e.g. on the right side of the figure or within courtyards), while higher surface temperatures up to 330 K are modelled at intensively irradiated vertical buildings walls. Moreover, the effect of different wall and roof material parameters on surface temperature can be identified, e.g. at roofs showing lower surface temperatures where green fractions are present, whereas some walls and roofs show values up to 320 K. In order to evaluate the modelled surface temperature more quantitatively, we compare the modelled surface temperature against observed values in the following section.

The observations cover a wide range of the street canyon configurations and surface types. A complete set of comparison graphs of the surface temperature for all points in all observation locations (see Fig. 1 in Sect. 2.1) for the summer e2 episode of the observation campaign (19–21 July 2018) and for the winter e3 episode (4–6 December 2018) is given in the supplements in Sect. S3. As a supporting information, the graphs of the modelled values of surface heat flux (shf), ground heat flux (ghf), net radiation (rad\_net), and incoming and outgoing shortwave (SW) and longwave (LW) radiation (rad\_sw\_in, rad\_sw\_out, rad\_lw\_in, rad\_lw\_out) are also available in the supplements in Sect. S4. The following subsections demonstrate the behaviour of typical urban environments and selected typical objects of the urban canopy.



**Figure 12.** Example 3D view of the child modelling domain with 2m resolution from west-south direction. The colour scale represents the modelled surface temperature on 20 July 2018 at 14:00 CET (13:00 UTC).

#### 4.3.1 Typical urban environments

530 The first selected typical situation represents a narrow street canyon of width between 10 and 20 m surrounded by traditional block-of-flats buildings with 4 to 6 stories over 20 m high (loc. 07, 08, 09; combination of LCZ 2 and 5 according to Stewart and Oke, 2012). Fig. 13 shows the situation for the location 07-2. The observations in the approximately south-north oriented street were done in the direction towards the west oriented (slightly south-inclined) wall.

In general, the modelled daily cycle of surface temperature agrees well with the observed surface temperature during the summer and winter episode. However, some discrepancies can be observed, e.g. during the summer e2 episode where the modelled surface temperature at 07-2\_H (pavement) shows slightly larger amplitude of the diurnal cycle (colder during the night, warmer in the daily maxima). At vertical surfaces, the modelled surface temperature agrees fairly well with the observed one during the summer episode. Throughout most of the winter e2 episode, the modelled temperatures at both horizontal and vertical surfaces are generally overestimated (up to 5 K on walls), where the model does not capture the night cooling on the first night and the model remains systematically above the observations for the rest of the episode. The horizontal surfaces also show a sharp peak around noon on 4 and 5 December, which does not appear on 6 December.

545 The next typical situation represents a wide street canyon with a combination of the traditional and the contemporary buildings (loc. 01, 02, 06, 11). Fig. 14 shows surface temperatures sampled at loc. 11-1 which is located on Evropská třída, the west-east oriented boulevard of width between 40 and 50 m (building to building width). The evaluation points are placed on the concrete tramway belt, pavement, and on the nearly south oriented wall of two traditional five-floor brick buildings with an additional thermal insulation layer in the case of the left one. For the summer scenario, the modelled surface temperature agrees fairly well at the horizontal and vertical locations with respect to the daily amplitude and temporal evolution. However, at the horizontal surfaces the modelled nighttime surface temperatures are underestimated by about 3–4 K. When the sun

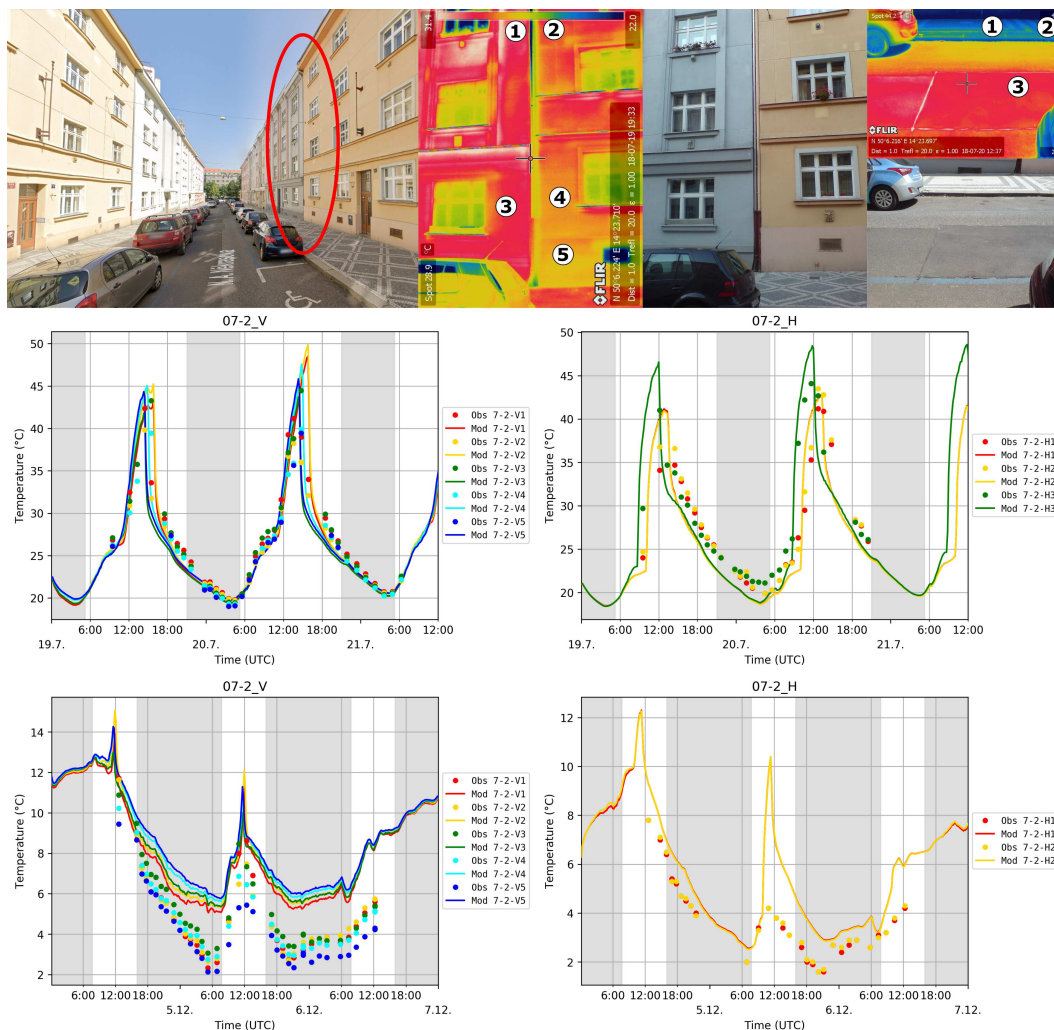


**Figure 13.** Observation location 07-2: the view of the observation location and IR and RGB photos with placement of the evaluation points (upper), observed (dots) and modelled (lines) surface temperature for wall (left) and ground (right) evaluation points for summer e2 (middle) and winter e3 (bottom) episodes. Top left image © 2020 Google.

comes-up the next day the modelled and observed surface temperature agrees fairly well again, meaning that the nighttime bias  
550 in surface temperature does not propagate to the next day. In the winter case the modelled surface temperatures also agree with  
the observations. At the second night where the surface temperature continuously decreases, the model shows values higher by  
1–2 K at both horizontal and vertical surfaces, while the modelled surface temperatures at horizontal surfaces match quite well  
with the observations in the following day and the third night. At the vertical locations, however, the modelled daytime surface  
temperatures show two sharp peaks during the morning hours as well as during early afternoon which were not captured by  
555 the observation. It strikes that the modelled surface temperatures at the vertical surfaces show also larger values (by about 2 K)



compared to the observation during the following night. However, compared to the summer case, the deviation of the modelled surface temperatures to the observed one is in a similar range.

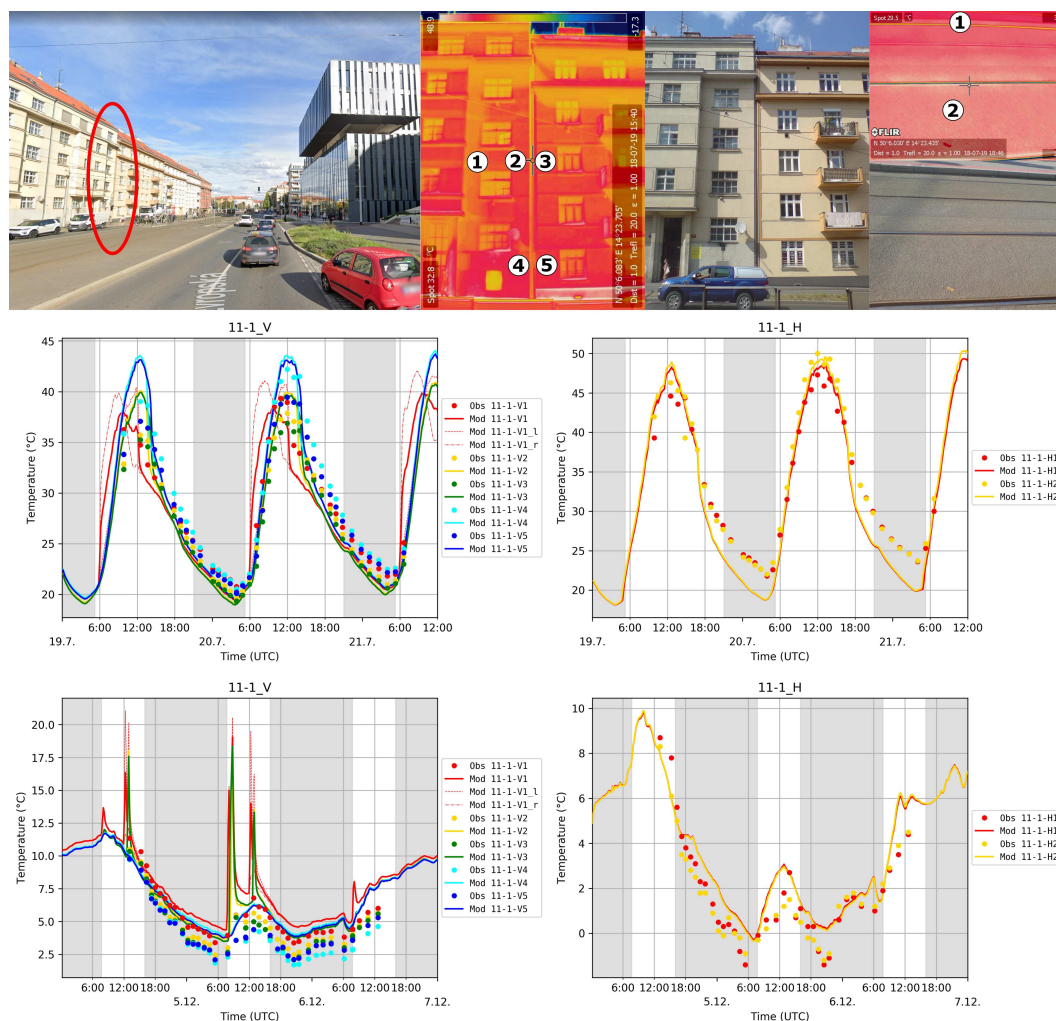


**Figure 14.** Observation location 11-1: the view of the observation location and IR and RGB photos with placement of the evaluation points (upper), observed (dots) and modelled (lines) surface temperature for wall (left) and ground (right) evaluation points for summer e2 (middle) and winter e3 (bottom) episodes. The dotted and dashed lines represent the modelled temperature for left and right grid faces (see description at the beginning of this section). Top left image © 2020 Google.

Location 12 covers a courtyard environment, representing another typical urban environment. The respective courtyard has a horizontal extent of approximately 160 m × 70 m and a depth of more than 20 m with large plant canopy inside the courtyard cavity. The observation points, depicted in Fig. 15, are placed on the south-southwest oriented wall of the Sinkule house student dormitory, which was built before World War II and has been insulated in the meantime. The ground points are located on the



565

asphalt/concrete playground near the building, the point 2 is influenced by large nearby trees. The model shows good agreement with the observations at the vertical surfaces during the summer episode, except for a slight underestimation of the diurnal cycle. Also at the horizontal surfaces the modelled surface temperature agrees well with the observed one, however, at nighttime the model underestimates surface temperature again. Compared to the summer case, the modelled surface temperature agrees less with the observed one for the winter episode. Here, the peak values at noon as well as the nighttime values are overestimated similarly to the previously shown two locations (see Fig. 13 and Fig. 14), which correlates with the overestimated global net radiation in this episode.

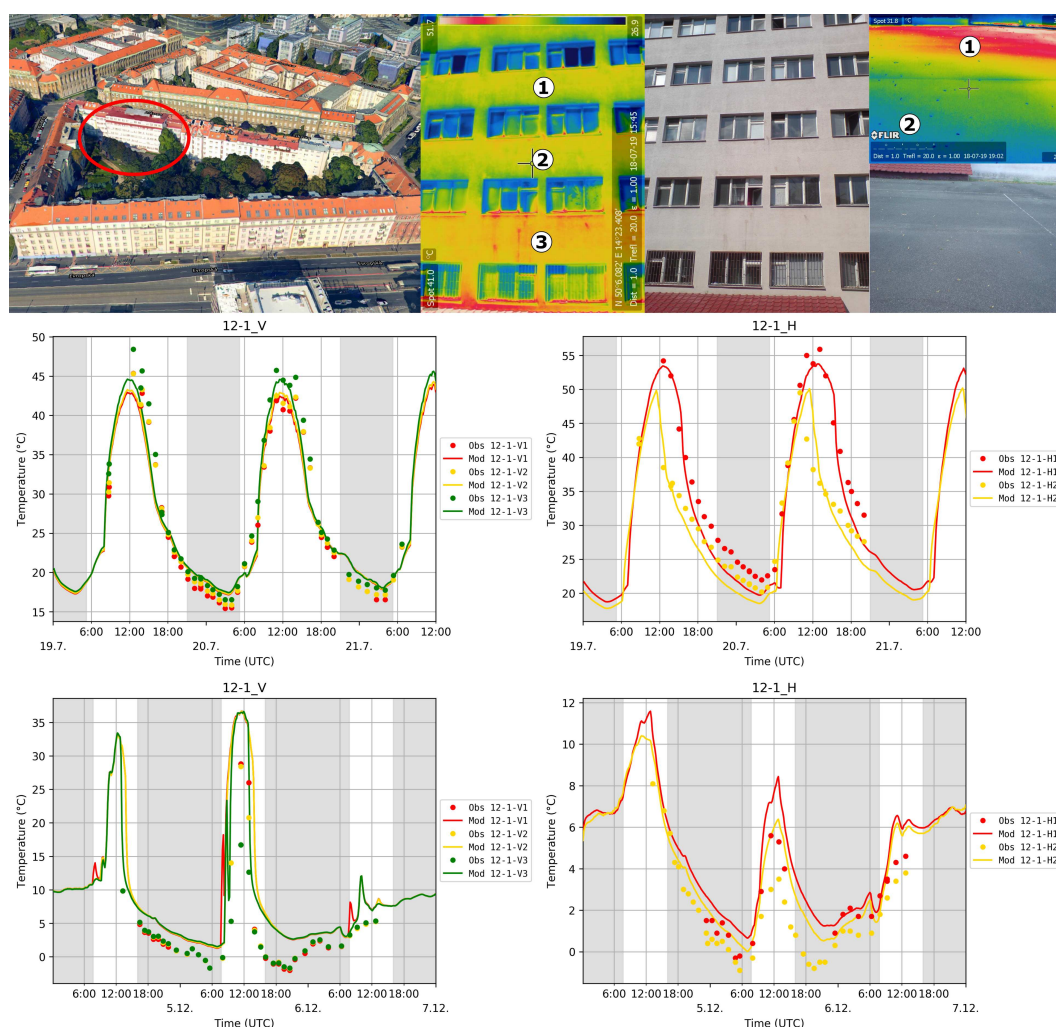


**Figure 15.** Location 12-1: the view of the observation location and IR and RGB photos with placement of the evaluation points (upper), observed (dots) and modelled (lines) surface temperature for wall (left) and ground (right) evaluation points for summer e2 (middle) and winter e3 (bottom) episodes. Top left image © 2020 Mapy.cz.



The last typical group of the urban environment which occurs in the studied area is represented by the relatively open places, such as a square or a park (locations 03, 04, 05, 10). Fig. 16 shows examples of the three types of pavement and grass on the central square Vítězné náměstí. The surface temperature at the pavement surface in location 10-1 is captured very well by the model during the summer episode, while during the winter episode the model tends to be warmer for the first two days of the observed period with overestimation of both daily minima and maxima. During the third day (6 December) the model is very close to the observations. The location 10-3 represents an example of the natural-like lawn. The diurnal cycle of the surface temperature agrees with observations well in both summer and winter episodes with slight underestimation of daily maximum on 19 July and overestimation of night temperatures during both summer nights.

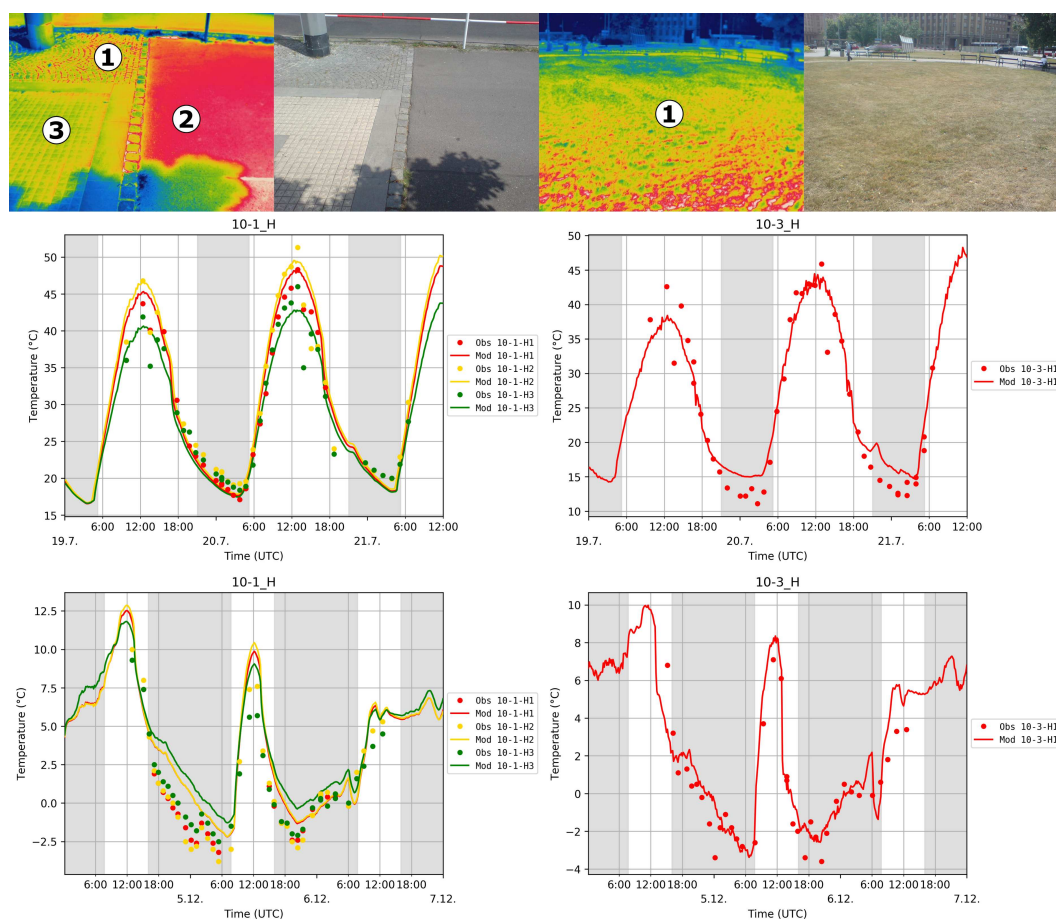


**Figure 16.** Location 10-1 and 10-3: the view of the observation locations and IR and RGB photos with placement of the evaluation points (upper), observed (dots) and modelled (lines) surface temperature for summer e2 (middle) and winter e3 (bottom) episodes.



### 4.3.2 Grounds modelling

The following sections describe behaviour of particular selected urban layer surfaces and objects across locations.

580 Pavements and streets belong to the most frequent types of ground surfaces in the urban environment. For a complete list of corresponding evaluation points see categories *pavements* and *streets* in Table S7. The agreement of model results with observations in case of pavements and streets is generally very good in most of the evaluation points. As an example see e.g. locations 10-1\_H (Fig. 16), 11-1\_H (Fig. 14), and point 12-1\_H1 (Fig. 15). Notable exceptions, however, are some locations influenced by trees (e.g. loc. 08, see Sect. 4.3.4).

585 Modelling of grass-covered surfaces represents a challenge. The energy balance of a grass-covered area may strongly depend on soil-water content, assumed plant cover, LAI, etc., which are mostly unknown in this study. A complete list of evaluation points placed on grass surfaces is provided in Table S7 in the category *grass*. Here, we examine points 05-1\_H3, 06-3\_H2, and 10-3\_H1 during the summer e2 episode (Fig. 17) which are not significantly influenced by any adjacent tree or wall. They represent examples of three different types of grass conditions. The first of them, 05-1\_H3 is placed in a recently built park with an integrated irrigation system, the second one 06-3\_H2 lays in a green tram line with shallow soil layer and without any watering, and the third point 10-3\_H1 is located in a quite large lawn in the open square area with deep soil layer without watering and thus resembling natural grass conditions. The daily cycle of the modelled and observed surface temperature at the different grass surfaces agrees fairly well with maximum temperatures of 35 °C, 52 °C, and 45 °C, respectively. Initial conditions of the soil were adopted from the WRF simulation which represents spatially aggregated values over various surface types. To model local differences in soil conditions properly, the grass areas within the model domain were split into three  
590 categories: natural-like grass, watered grass, and urban grass type, while the original WRF soil moisture was adjusted by factors 1.0 (e.g. 10-3\_H1), 2.0 (e.g. 05-1\_H3), and 0.5 (e.g. 06-3\_H2), respectively for summer simulations. The soil moisture for winter simulations was not adjusted. Fig. 17 also shows daily cycles of surface temperature at point 06-3\_H2 (tram line) and 05-1\_H3 (irrigated park) from a test simulation where the soil moisture of grass surfaces was uniformly prescribed from the WRF simulation. With non-adjusted soil moisture, the daytime surface temperature at point 06-3\_H2 and 05-1\_H3 is under-  
600 and overestimated compared to the observed one, respectively, while it agrees fairly well for the adjusted soil-moisture case. This indicates that using correct soil moisture values is a necessary prerequisite to sufficiently model natural-type surfaces within urban environment. Sensitivity of the model to the initial soil moisture is investigated in Belda et al. (2020). Apart from soil moisture, sensitivity of grass surface temperatures on other parameters such as LAI, plant cover, root-distribution, etc., might also be important and needs further investigation.

### 605 4.3.3 Wall surface modelling

Buildings represent an essential element of the urban canopy and they influence the street canyon environment substantially. Heterogeneity of building types and properties is usually higher than in case of ground surfaces. Heterogeneity of properties of building walls is also very high due to windows, ledges, balconies, stuccoes, and other facade objects. Moreover, determination

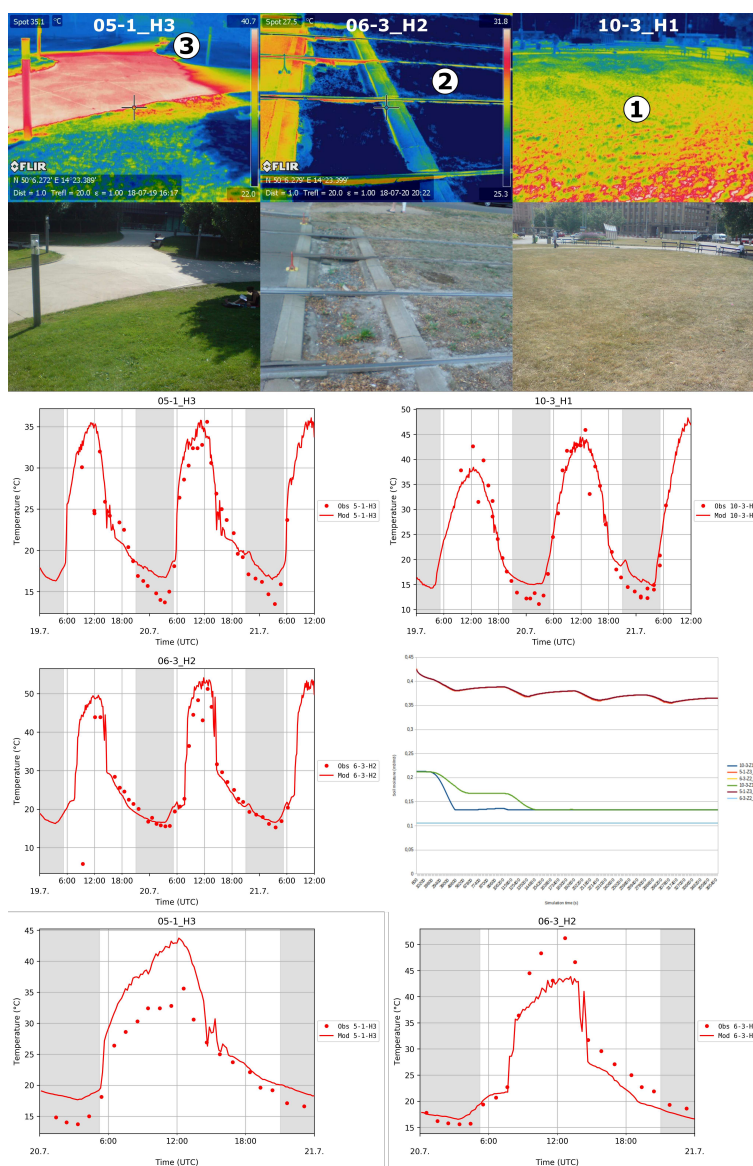


**Figure 17.** IR and RGB photos with evaluation points 05-1\_H3, 06-3\_H2, and 10-3\_H1 (upper) which represent three different grass types found in the modelled urban area. Observed and modelled surface temperature at these locations. Middle right graph shows the time development of soil moisture in the first two PALM soil layers during the simulation of episode summer e2. Two lower graphs show results from testing one-day simulation with all grass surfaces initialized with soil moisture uniformly prescribed from WRF simulation for evaluation points 05-1\_H3 and 06-3\_H2.



of building wall and roof properties is usually a very difficult process even in case of a detailed field survey. Nevertheless, we  
610 can roughly distinguish a few basic building categories in the studied domain.

The first category represents traditional buildings built from insulated bricks or construction blocks or poured concrete with  
various types of plaster and occasionally provided with additional surface insulation. A complete list of evaluation points placed  
on such types of walls is given in Table S7 under the *wall* (traditional building) category. The agreement of model results with  
observations for this type of walls is usually very good and occasional deviations can be attributed to the inaccuracy of the wall  
615 parameters. As an example, Fig. 18 shows the surface temperature for evaluation point 06-4\_V. For the summer episode the  
modelled and observed surface temperature agree fairly well. For the winter episode the situation is different. On the first day  
the modelled and observed surface temperature agree. During the first night, however, the wall cools down less rapidly in the  
model compared to the observation, being about 5 °C warmer in the model, which is in accordance to the other locations where  
WRF / PALM is not able to capture the nighttime cooling. Even though the modelled surface temperature is overestimated  
620 on the following day and night, the daily cycle and amplitude of surface temperature is well captured by the model on the  
following day, indicating that PALM is able to sufficiently simulate the physics at such wall surfaces.

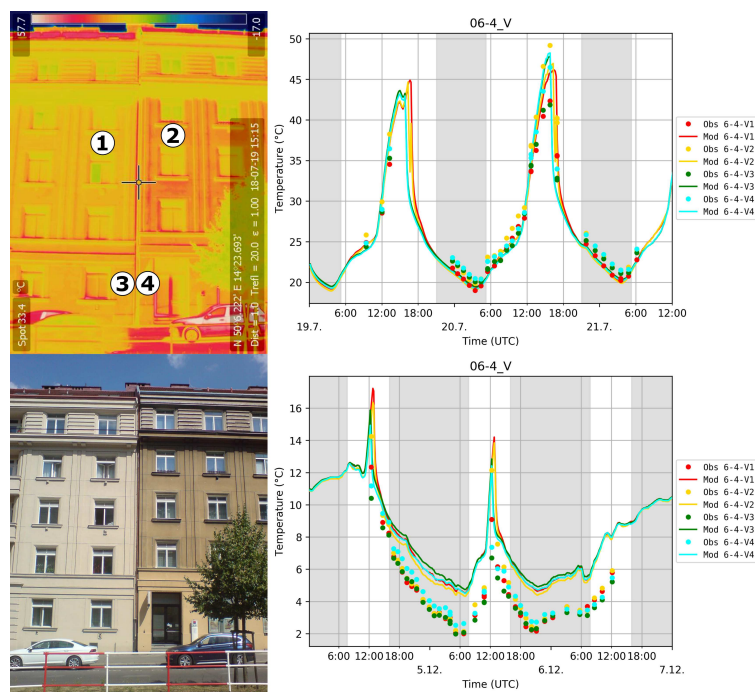


**Figure 18.** Location 6-4\_V: IR and RGB photos of the observation location with placement of the evaluation points (left), observed (dots) and modelled (lines) surface temperature for summer e2 (top right) and winter e3 (bottom right) episodes.

The next group of buildings includes the modern type of large buildings characterized by steel or steel/concrete skeleton and prefabricated walls with a complex layer structure. A complete list of evaluation points of this type is provide in Table S7 in category *wall* (*contemporary office building*). The agreement of model results with observation is variable and usually lower



625 for this type of surfaces. This can be attributed to a more complex structure of wall layers which is not fully described by the  
current version of the BSM wall heat model. Additionally, gathering precise information about this type of structure proved  
to be more difficult. An example evaluation for points 02-3\_V1 and 02-3\_V2 is shown in Fig. 19. While the point 02-3\_V1  
is captured by the model quite well except for slight overestimation during the night and morning hours, the point 02-3\_V2  
evinces an overestimation of around 15°C during the afternoon hours. A closer direct inspection of this wall revealed that the  
630 wall consists of a thin upper layer followed by 10 cm thin air layer and then followed by the rest of the wall structure, while  
the model considered this as a continuous wall. The observed outermost layer thus was cooled from both sides which was not  
modelled properly by the current wall model.

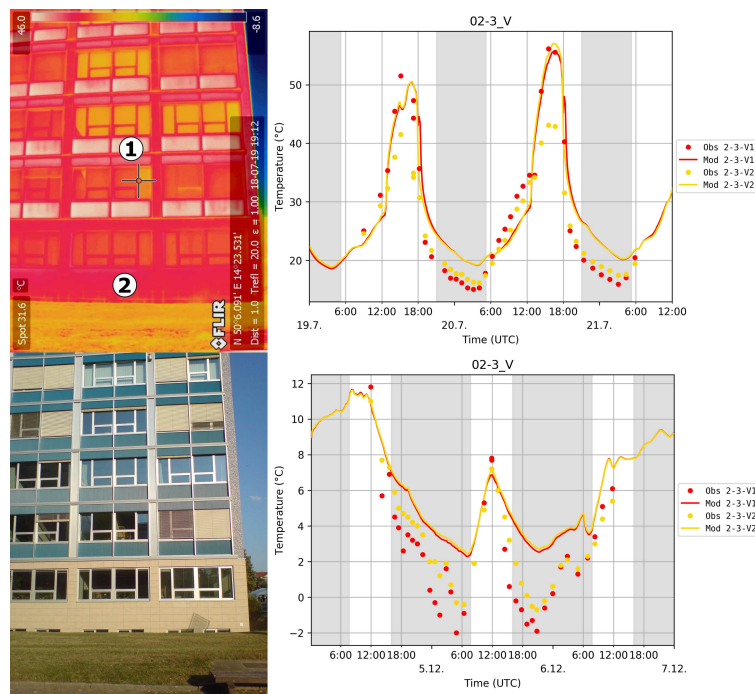


**Figure 19.** Location 02-3\_V: IR and RGB photos of the observation location with placement of the evaluation points (left), observed (dots) and modelled (lines) surface temperature for summer e2 (top right) and winter e3 (bottom right) episodes.

A third important category of the buildings in the modelling domain is represented by contemporary office buildings with similar skeleton as in previous category but with surface constituted of glass or glass-like materials. Evaluation points belonging  
635 to this type are summarized in Table S7 as the category *wall (glass like surface building)*. As an example, the location 11-2\_V is shown in Fig. 20. At daytime the modelled surface temperature agrees well with the observed one, whereas at nighttime the model shows significantly higher surface temperatures compared to the observation. However, we note that such a kind of building presents a challenge for both observation and modelling. The surfaces of the buildings are more or less specular and this fact causes that the IR camera observations contain substantial part of the LW radiation reflected from an opposite  
640 object as can be seen on IR image in Fig. 20. For example, the glass surface of the building around the evaluation point 11-



2\_V2 reflects the sky, while around the evaluation point 11-2\_V3 the glass surface reflects the opposite building (location 11-1\_V). Consequently, the derived surface temperature represents primarily the surface temperature of the reflected object (wall, ground, treetop, sky), not the observed object itself and thus this type of building cannot be considered as validated by this study.

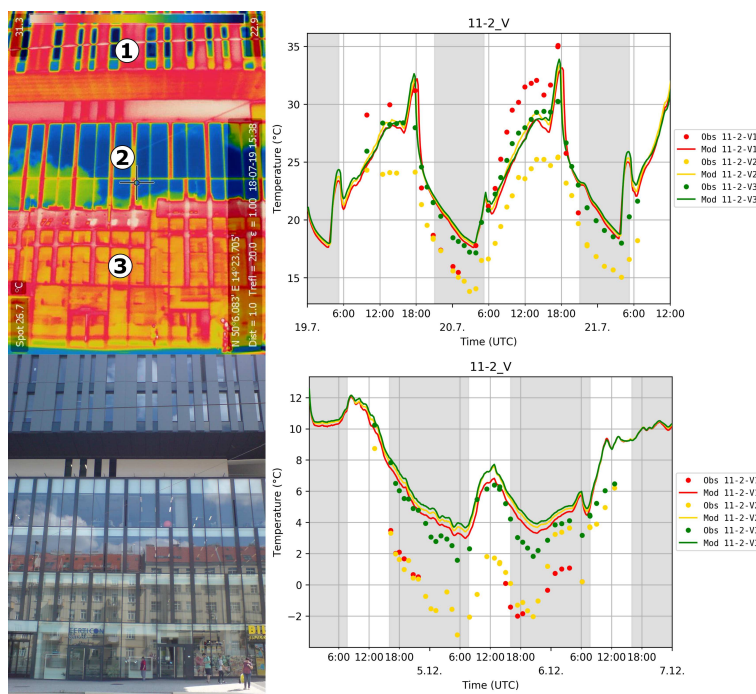


**Figure 20.** Location 11-2\_V: IR and RGB photos of the observation location with placement of the evaluation points (left), observed (dots) and modelled (lines) surface temperature for summer e2 (top right) and winter e3 (bottom right) episodes.

645 From the modelling point of view, specular reflections are not considered by the current version of RTM, which considers all reflections to be Lambertian (see Krč et al. 2020). This affects the distribution of reflected SW and LW radiation among nearby surfaces. An example of this can be seen in point 06-1\_H2 in comparison with point 06-1\_H3 (see Fig. 21). These points are placed on similar asphalt concrete surfaces but with different distance to the nearby glass facade. While the surface temperature at the more-distant point 06-3\_H3 is modelled well, it is underestimated by about 7 °C at point 06-3\_H2 on 20  
650 July 2018 at hours 11-13 UTC, which we attribute to the specular reflection of the glass facade which is not considered in the model. In reality, point 06-3\_H2 receives more SW radiation by specular reflection of the direct sunlight from the glass facade before noon, so that the pavement can heat up. However, by assuming that all reflections are Lambertian in the RTM, we do not account for the additionally reflected SW radiation from the glass facade, resulting in less available energy to heat up the surface. The other point 06-1\_H1 (limestone pavement) is less affected by the missing specular radiation due to its much higher  
655 albedo.

Validation of wall heat flux is discussed in Sect. 4.4 and it provides additional information for the wall modelling.

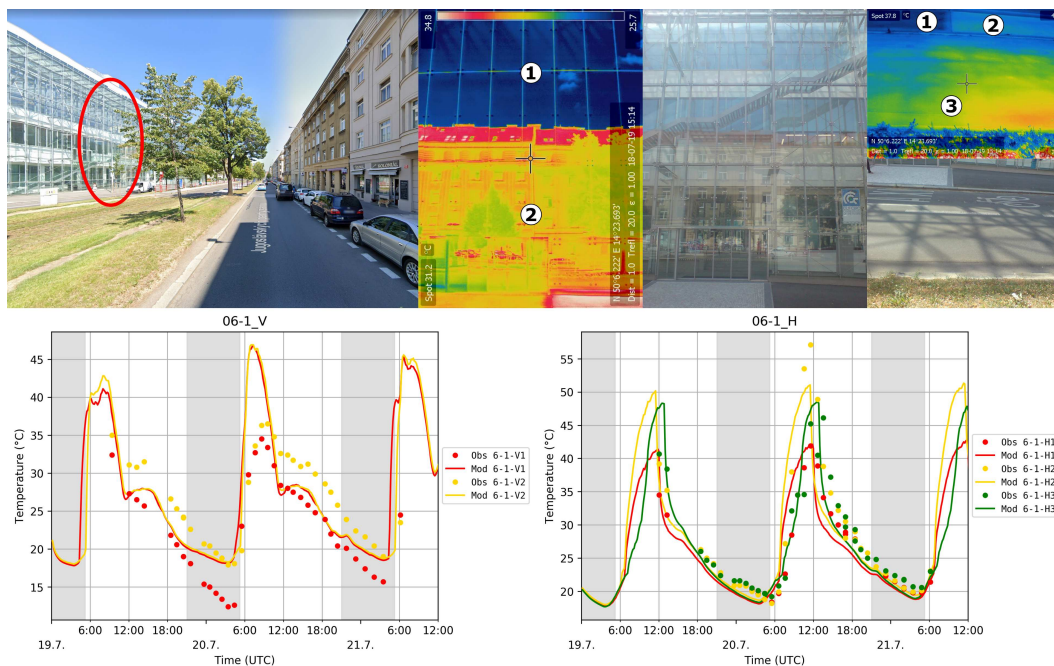


**Figure 21.** Location 06-1: IR and RGB photos of the observation location with placement of the evaluation points (top), observed (dots) and modelled (lines) surface temperature for summer e2 episode (bottom). Top left image © 2020 Google.

#### 4.3.4 Plant canopy modelling

Trees and shrubs are modelled in PALM as the resolved plant canopy (PC) which is described by a fully 3D structure of leaf area density (LAD). Beside affecting the turbulent flow by adding LAD-dependent drag, resolved plant canopy also affects the radiative transfer by partially intercepting SW and LW radiation as well as emitting LW radiation. Further, the absorbed incoming radiation is transformed into latent and sensible heating terms which are considered within prognostic equations of potential temperature and humidity. Many evaluated points are more or less affected by some PC. A list of evaluation points where significant impact of PC can be seen is given in Table S7 in row plant canopy affected surface. Here we focus only on the summer scenarios since deciduous trees (which constitute the majority of the trees in the domain) carry no leaves during the winter. Impact of the branches during the winter episodes is roughly modelled as 10 % of the summer LAD.

The first two examples (see Fig. 22 and 23) show a situation of two points placed on the same surface (cobblestone and asphalt concrete, respectively) where point 2 is directly influenced by the tree shading while tree influence on the point 1 is much lower. The shading of the treetop decreases the surface temperature after noon, which is well considered by the model.

The last example (Fig. 24) shows asphalt/concrete and cobblestone surfaces placed in a street canyon with two alleys of trees with linked treetops forming an umbrella-like covering. The street surface temperature is underestimated by the model up to 5 °C. While these surfaces are modelled well in other locations, a possible explanation for this discrepancy could be the tree

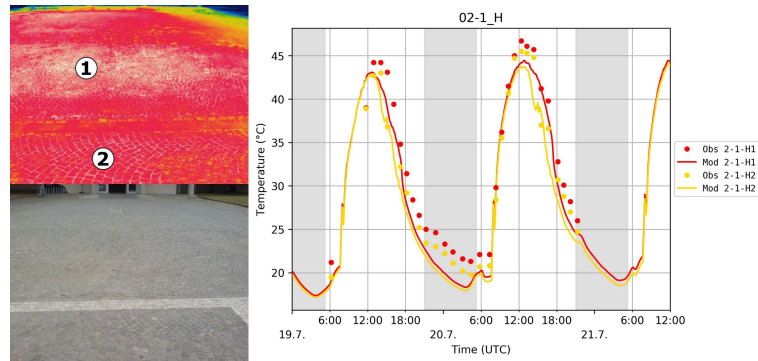


**Figure 22.** Location 02-1\_H: IR and RGB photos of the observation location with the placement of the evaluation points (left) and observed (dots) and modelled (lines) surface temperature for summer e2 episode (right).

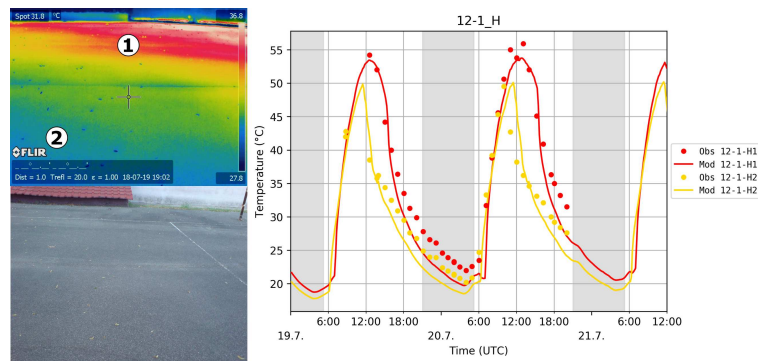


**Figure 23.** Location 12-1\_H: IR and RGB photos of the observation location with the placement of the evaluation points (left) and observed (dots) and modelled (lines) surface temperature for summer e2 episode (right).

shading. The large tree crowns tend to arrange themselves into clusters with free space between them (see e.g. Mottus, 2006) with spots of direct shortwave radiation as Fig. 24 suggests that this is also the case. As this fact was not taken into account in generation of tree input data, the resulting homogeneous LAD overestimates the shading of the radiation in the simulation.

#### 675 4.3.5 Discretization issues

PALM discretizes the domain in a Cartesian grid where all values in every grid box are represented by one value. This leads to standard discretization errors. Moreover, the current version of PALM uses the so-called mask method to represent obstacles (terrain, buildings), where a grid box is either 100% fluid or 100% obstacle and consequently any surface is represented by orthogonal grid faces (see. Fig. 4). Besides implications with respect to the near-surface flow dynamics and an increase of  
 680 effective roughness, a step-like representation also increases the total surface area, modifies the direction of the normal vector and the mutual visibility of the particular grid surfaces, which in turn also affects the surface net radiation and thus the surface

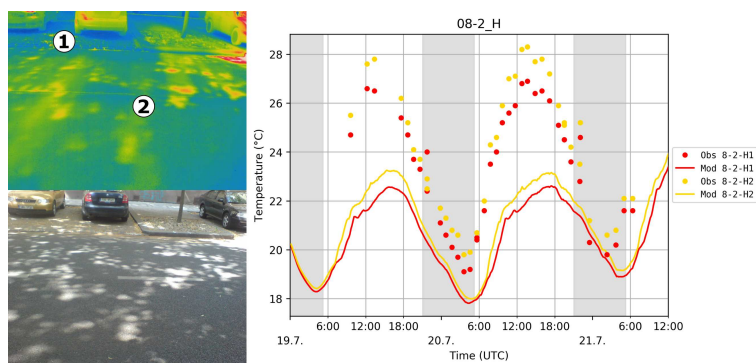


**Figure 24.** Location 08-2\_H: IR and RGB photos of the observation location with the placement of the evaluation points (left) and observed (dots) and modelled (lines) surface temperature for summer e2 episode (right).

energy balance. The observations of the surface temperature allow to demonstrate a few selected implications on radiative transfer and surface energy balance.

The first observed consequence of the discretization is the fact that the subgrid-size surface features cannot be represented, while in reality, these objects can significantly influence the shading of the wall (e.g. Fig. 25). This effect needs to be taken into account in point comparison of the related surface values.

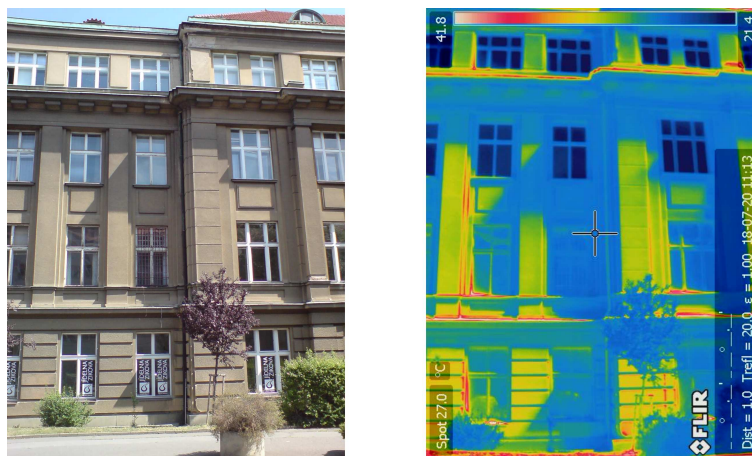


**Figure 25.** Camera RGB (left) and IR (right) photo of the wall of the building in the Zikova street (location 01-1\_V) on 20 July 2018 at 10:13 CET.

The next important effect caused by the step-like representation of the surface is the artificial shading. This effect can be observed in case of “slope” terrain or walls (“slope” in case of walls means non grid-aligned walls, i.e. walls which are oriented in one of the south-west, south-east, north-west, and north-east directions and which are approximated by step-like structures).

Fig. 26 shows an example of the modelled surface temperature in the park around location 05-1\_H. Terrain of the park is



slightly declining in the south direction which causes three artificial “steps” in the gridded representation of the terrain, one near the building, next in the centre of the park, and last near the south side of the park. The induced artificial shading causes significant drop of the surface temperature in affected surface grid cells which is well visible in the figure and which has no counterpart in reality. Other grid surfaces which are not directly influenced by artificial shading are also affected by the discretization of the terrain. The gridded ground surface is oriented horizontally while the real terrain surface is inclined about 4° to the south. This inclination decreases the incoming direct SW radiation by about 4 % in case of situation presented in Fig. 27 and even more for other hours of the day when sun elevation angle is lower. As a consequence, the incoming radiation and surface temperature in the model are overestimated for these surfaces. A demonstration of this effect can be done on evaluation points 03-1\_H1, 04-1\_H1, and 05-1\_H2. These points lay on exactly the same type of the surface and none of them is directly influenced by any building or tree. While the modelled and observed surface temperature agree well in the first two cases, the modelled temperature in point 05-1\_H2 is overestimated about 4 °C during the day (see Fig. 27), which supports our hypothesis that the missing sloped-surface representation in the model causes this bias.

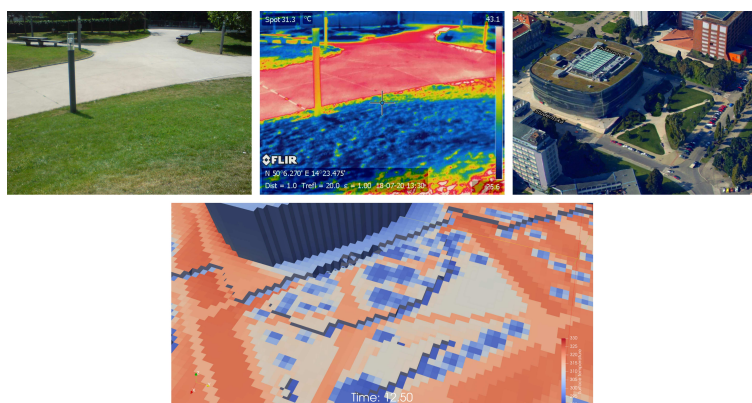


**Figure 26.** The park beside the building of Technical library (location 05-1) on 20 July 2018 at 12:30 CET. RGB (upper left) and IR (upper middle) photo of the location, 3D view on modelled surface temperature in this location (bottom) and an illustrative aerial view of the location. Top right image © 2020 Mapy.cz.

An example of the transformation of the buildings from GIS data to a grid structure and of the impact of this structure on the resulting surface temperature for Sinkule dormitory (location 12-1) is shown in Fig. S18. The effects of the artificial shading as well as the alteration of the surface normal vector can be illustrated on the wall around the observation location 07-1 (see Fig. 28). This wall is oriented to the east with slight inclination to the north. The upper pictures show the observed photo on 20 July 2018 at 10:37 CET and 3D view of the modelled incoming SW radiation on this wall at the corresponding modelling time step. The bottom pictures show the same situation approximately one hour later at 11:38 CET. In the first case, the wall is irradiated by the direct sun radiation and the model result shows the artificial shading of some grid faces caused by the step-like representation of the wall. The second case shows the situation when the wall is shadowed in the reality but some corresponding modelled grid faces are irradiated by direct sun radiation due to their turn to the east direction.

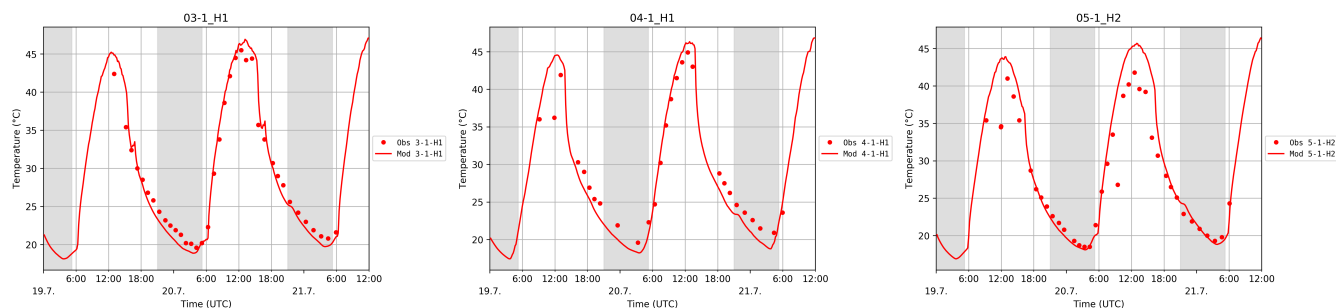


**Figure 27.** Observed (dots) and modelled (lines) surface temperature at points 03-1\_H1 (left), 04-1\_H1 (middle) and 05-1\_H2 (right) for the summer e2 episode.

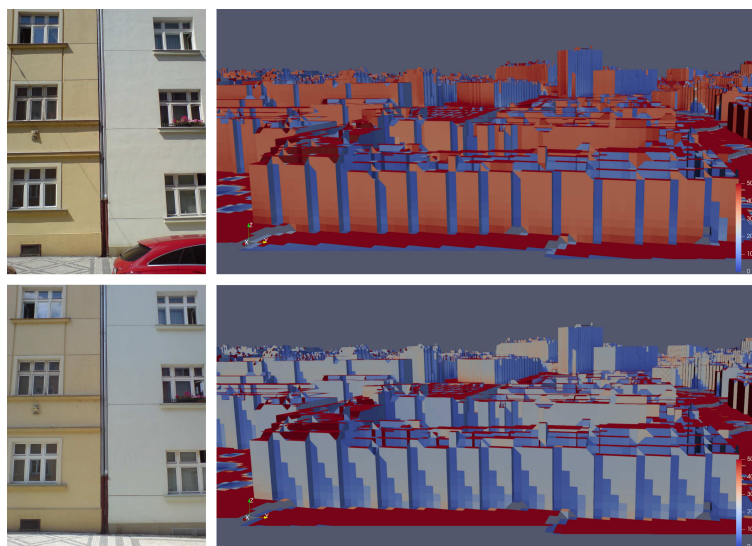


**Figure 28.** East facing wall in the street of N. A. Někrasova around location 07-1\_V. The top row shows the observed photo on 20 July 2018 at 10:37 CET and the 3D view of the modelled incoming SW radiation on this wall at corresponding time step. The bottom row shows the same situation at 11:38 CET.

Next two consequences of the orthogonally gridded model surfaces are altered distribution of the reflected radiation and artificial self-reflections owing to the step-like terrain and wall representation. The first effect is difficult to demonstrate in the observed data due to less direct attribution of the reflected radiation to the particular source surface and its partial masking by the stronger direct radiation. The second effect can be best tracked on the sloped roofs but they were not observed within this observation campaign. It can also be demonstrated on the walls e.g. on the wall around the location 07-2\_V on the 20 July 2018 at 11:37 CET (see Fig. 29). The wall is not irradiated in reality by the direct sun radiation at this moment. The south facing model wall grid faces are illuminated by the direct radiation and the radiation reflected from them consequently irradiates adjacent grid faces turned to the west.

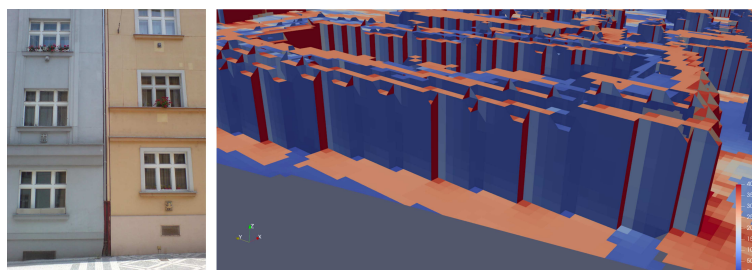


**Figure 29.** West facing wall in the street of N. A. Někrasova around location 07-2\_V. The figure shows observed photo on 20 July 2018 at 11:37 CET (left) and the 3D view of the modelled incoming SW radiation on this wall at corresponding time step (right).

720 These potential sources of problems need to be considered, especially, due to its local nature, for point-to-point comparisons  
of modelled and observed quantities. However, in case of averaging over larger areas, these artificial effects partially mutually  
compensate due to the fact that the global amount of the incoming direct and diffuse radiation, which represents the strongest  
radiation forcing, is similar on the original and discretized surface. This will make these artificial effects less important for  
practical model utilization than in case of the model point evaluation. Some potential amends in the model are discussed in  
725 Sect. 5.2.

#### 4.4 Wall heat flux

The observations of the wall heat flux (HF) in two locations (see Sect. 2.3.2) allow direct comparison with the wall heat flux  
simulated by the model. Moreover, the observations of the surface temperature from the sensor allow to validate the PALM  
model as well as the observations obtained by the IR camera.

730 During the summer campaign, the HF observations took place in Sinkule house from 19 July to 3 August 2018 and in  
location Zelená from 3 to 7 August 2018. This period overlaps only partly with modelling episode summer e2. The graphs of  
heat flux and surface temperature are shown in Fig. 30. The modelled and observed wall heat flux on the ground floor shows  
a similar daily cycle with a similar amplitude, though the model slightly overestimates the observed values by about 5 to 10  
 $\text{W}\cdot\text{m}^{-2}$ , while the corresponding modelled surface temperature agrees fairly well with the observations. The modelled wall heat  
735 flux on the first floor shows a pronounced daily cycle, while the observed wall heat flux shows only a weak daily cycle with a  
significantly smaller amplitude. The modelled surface temperature, however, shows a smaller amplitude with higher nighttime  
but lower daytime temperatures compared to the observation, which is in agreement to the respective wall heat fluxes where  
the model increasingly partitions the available energy into the wall heat flux.

The winter HF observations at the Sinkule house cover the episode e3 from 4–6 December 2018 and the observations in  
740 location Zelená fit to episode e2 in days 27–28 November 2018 (see Fig. 31). Even though the modelled surface temperature  
at the Sinkule house for the ground floor observation is slightly overestimated on the second day with respect to the observed  
one, the modelled and observed wall heat fluxes agree fairly well during the shown period. In contrast, on the first floor the  
modelled wall heat flux (absolute value) and surface temperature are strongly overestimated, especially during the nights.

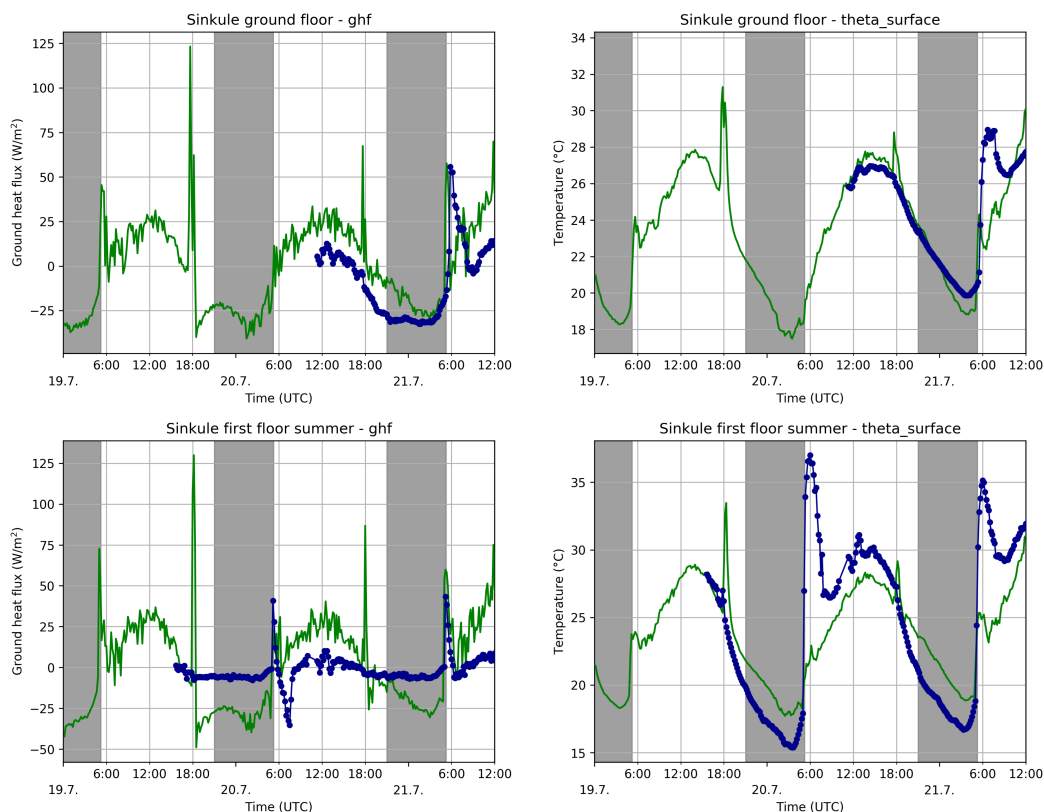


**Figure 30.** Modelled (green) and observed (blue) wall heat flux (left) and surface temperature (right) for days 19–21 July 2018 for location Sinkule house at the ground floor wall (upper) and at the first floor wall (bottom).

The minimum of the modelled wall heat flux reaches down to  $-50 \text{ W.m}^{-2}$  during the night from 5 December to 6 December while observations suggest values between  $-10$  and  $-15 \text{ W.m}^{-2}$ . The situation in location Zelená is similar; the modelled HF fluctuates around  $-40 \text{ W.m}^{-2}$  during nights while the modelled counterpart reaches down to  $-80 \text{ W.m}^{-2}$ . This behaviour suggests that the thermal wall resistance in case of higher floors of the buildings Sinkule house and Zelená are underestimated. Both locations are older buildings which had been insulated in the past except for the ground floor. The real thermal resistance of this additional insulation layer, which is set in the input data to approximately 6 cm of polystyrene, is probably underestimated.

#### 750 4.5 Street canyon meteorological quantities

Data collected by the mobile meteorological stations and vehicles allow us to compare the main variables characterizing the atmospheric properties inside several street canyons. A large spatial variability inside a street canyon is expected and predicted by LES, therefore perfect agreement of the simulation and measurement cannot be expected. The comparisons also contain values from the WRF simulation to allow to assess the contribution of the micro-scale model. This section presents a

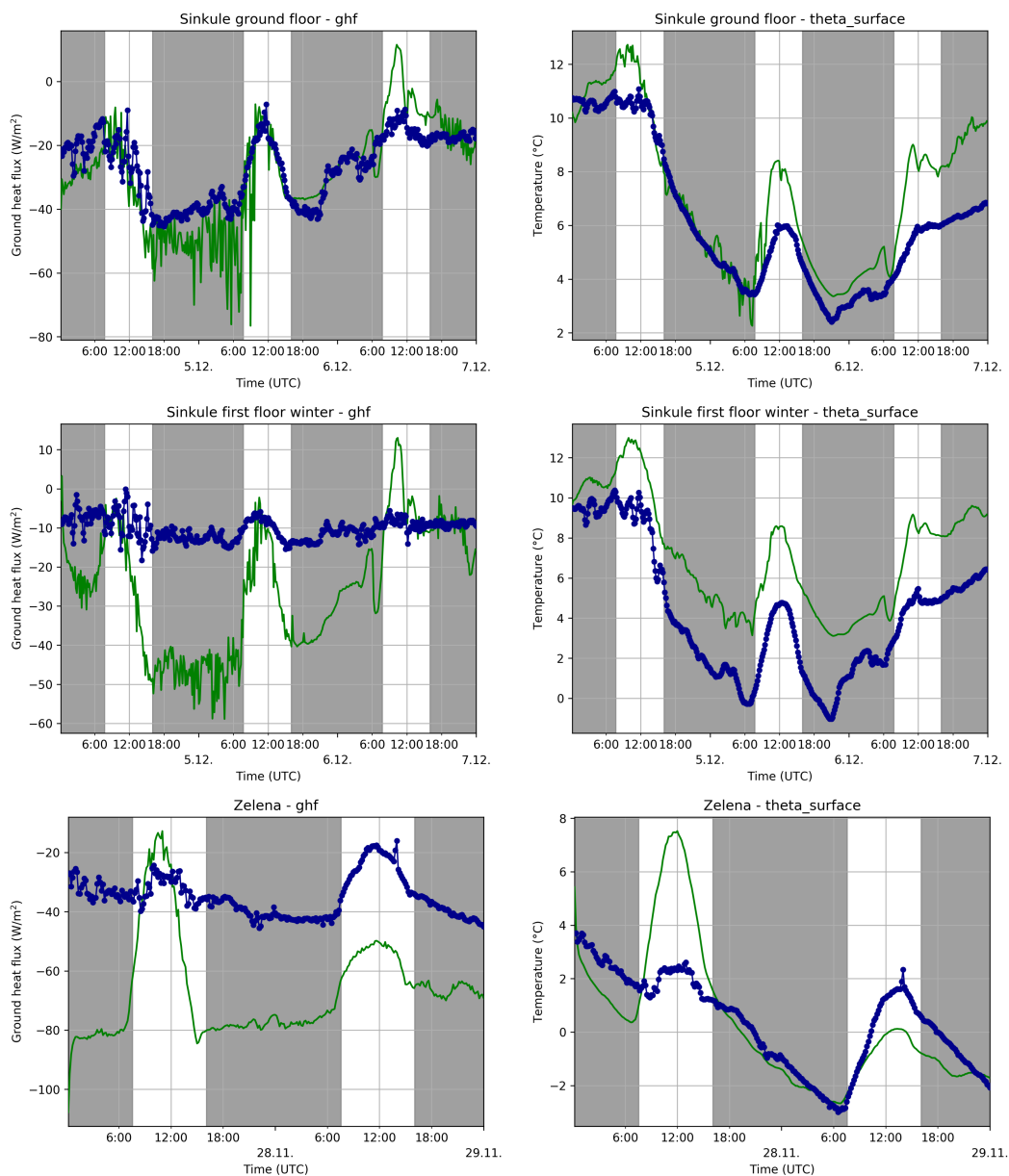


**Figure 31.** Modelled (green) and observed (blue) wall heat flux (left) and surface temperature (right) at days 5–6 December 2018 for location Sinkule house at the ground floor (upper) and at the first floor (middle) and at location Zelena at days 27–28 November 2018 (bottom).

755 comparison of the modelled temperature and wind speed with observations. Vertical sensible heat flux, relative humidity, and wind components can be found in the supplements in Fig. S19, Fig. S20, Fig. S21, and Fig. S22 respectively.



#### 4.5.1 Air temperature

Graphs of the air temperature at 3.9 m (Sinkule house) and 4.6 m (other locations) are plotted in Fig. 32. In the summer campaign, the diurnal cycle is generally well resolved with daily maximum temperatures agreeing better than the daily minimum temperatures. The nighttime cooling is most often underestimated and hence the minimum temperature is too high. However, on certain days, e.g. on the 16 July, the simulated minimum temperature is lower than the observed one. The maximum temperature on the previous day was also higher than the simulated one. The comparison with the WRF 2m temperature in the closest point shows that on several days the WRF modelled temperature agrees to the night street-canyon observations more closely. During the summer campaign the global radiation is well predicted by WRF except 23 July, which, however, coincides with the break in the episodes and movement of the measuring vehicles.

During the winter campaign, the simulated air temperature follows the observations less reliably. The behaviour changes during the simulated period. In episode 1, the daily peak temperatures are overpredicted. On the second day of the episode, the observed temperature during the day is stationary while it significantly rises in the model. The cooling at the end of the episode is captured correctly. However, it strikes that PALM mostly follows the daily cycle simulated by WRF.

During the winter e2 episode, the temperature evolution is characterized by significant nighttime cooling. This is reflected in the model, though with a much weaker intensity. On the first day the daytime temperatures are also overpredicted which is in accordance to the strong over-prediction of the global radiation by WRF (Fig. 5). PALM closely follows the temperatures in WRF during the episode. That can also be observed in episode e3 where the cooling on the night from 4 to 5 December is well reproduced except the last few hours. After well predicted daytime temperatures and an over-predicted night, the episode ends with an increase of temperature for 24 hours, which is overpredicted. That is again likely related to the over-predicted global radiation in WRF on 6 December (Fig. 10).

#### 4.5.2 Wind speed

The simulated and observed wind speed in the respective street canyons for the summer campaign generally show good agreement, even though they also indicate significantly larger wind speeds in the model at both Orlík locations (see Fig. 33). These locations also show large spatial gradients in the form of a large spread of the simulated wind speed in the neighbouring grid points (the shaded band in Fig. 33). That means that the spatial representativeness of the point measurement is limited and that the simulated values are very sensitive to the exact position of the sampling. The observing vehicle was located close to the wall. The large trees in the Terronská street, where Orlík stations were located, also increase the uncertainty, where the trees at top have a radius of 2 m in the model, but a radius of about 5 m in reality (see Fig. S7). This discrepancy could have also influenced other modelled variables. For other locations, the wind speed in the street and courtyard locations generally agree well with the observations.

In the winter campaign the behaviour is more complicated. Episode 1 is very calm which is also reflected in the simulations. The comparisons at the Orlík stations in episode 2 are affected by the same factors connected with the spatial representativeness and tree size as in the summer campaign. Most of the episode 2 still shows a good agreement at Sinkule house, but the night

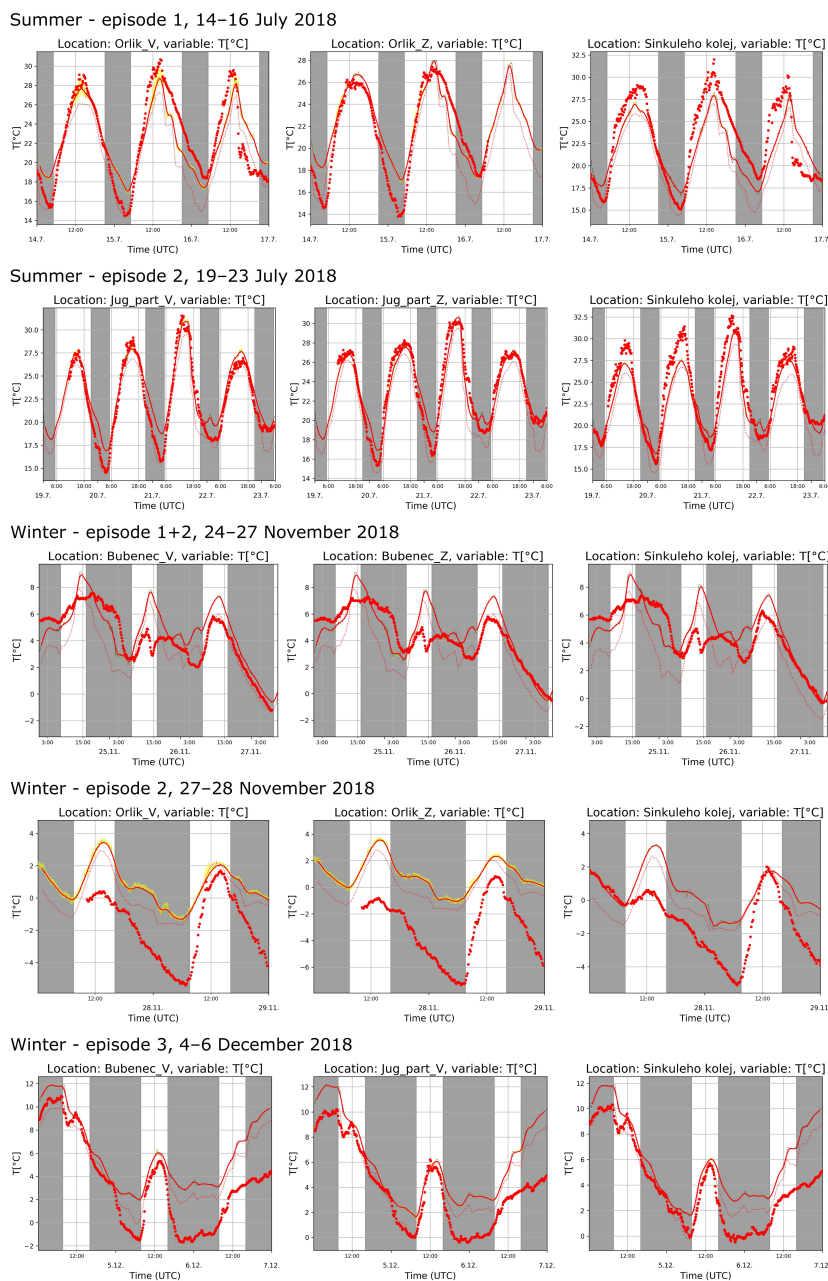


**Figure 32.** Modelled (solid red line) and observed (red dots) temperature in particular street canyon observation locations. The solid red line represents the one-hour moving averages while the thin black line shows the original 10-minutes averages. The yellow band denotes the interval between the smallest and the largest 10-minute average value among the neighbouring grid points. The thin dotted red line indicates corresponding value from WRF simulation.



790 to 29 November shows an increase of wind speed which cannot be observed in the measurements. The increase in wind speed is in accordance to the simulated wind speed in WRF and is connected with an occluded front passing the area. Episode 3 is variable with moderate overestimations at certain times. The overestimations on 4 December can be linked to the inaccuracies in the whole wind profile and hence the boundary conditions from WRF in Fig. 10.

#### 4.6 Street canyon air quality quantities

795 This section presents a comparison of modelled and observed concentrations of  $\text{NO}_x$ . The results for  $\text{PM}_{10}$  can be found in the supplements in Fig. S23. Figure 34 shows the simulated and measured concentrations of  $\text{NO}_x$  in the summer and the winter campaign. In general, the modelled concentrations show a similar magnitude and indicate a similar temporal evolution as the measurements. It strikes that the simulated concentrations are closer to the measurements in the summer cases, even though also in the summer cases concentrations temporally deviate from the measured values significantly, e.g. during nighttime and  
800 the morning hours on 15 July where concentrations are significantly underestimated. In the evening of 15 July, there was a large concentration peak simulated, but no peak can be observed in the measured data which becomes especially apparent at the Sinkule house station where the scatter of the observed concentrations is only small within the enclosed courtyard cavity. Another large overprediction of modelled concentration can be observed in the morning of 21 July. Also, for both these overpredictions, the CAMx mesoscale simulation shows larger concentrations compared to the measurements in the courtyard.  
805 A possible reason for temporal mismatch of modelled and observed concentration might lie in the different wind speeds. The modelled wind speed profiles are significantly lower compared to the observed wind speed from the aerological soundings at 06:00 UTC 21 July (Fig. 33), especially near the surface. At midnight on 21 July, both the modelled and the observed wind profiles indicate a well pronounced low level jet near the surface. Later during the morning hours, the low-level jet can still be observed in the measured profile, while it is not present any more in the modelled profile, accompanied with lower wind speeds  
810 and less mixing near the surface, which in turn favours the built-up of higher concentrations in the model.

In winter, the modelling of  $\text{NO}_x$  concentrations is complicated by local heating and the associated uncertainties of the emissions. The strong simulated peak in the morning of 25 November, which is also present in the CAMx results, does not appear to be present in the measurements at all. A detailed examination of the concentration fields show a strong effect of the local heating sources and also the effect of the boundary conditions.

815 The validation metrics according to Britter and Schatzmann (2007) and Chang and Hanna (2004) for the summer and the winter campaign are summarized in Table 2. The statistics were computed from all available 10-minute concentration averages in all points where measurements were available. The metrics fulfil the criteria for dispersion models as suggested by Chang and Hanna (2004). Namely the bias is less than 30 %, the modelled values fit within the interval given by the half and the double of the observed value more than 50 % of the time and the random scatter is within the factor of one of the mean value.  
820 The performance in the summer campaign and in the winter campaign only differs in the sign of the fractional bias which is negative in summer (overpredictions) and positive in winter (underpredictions).

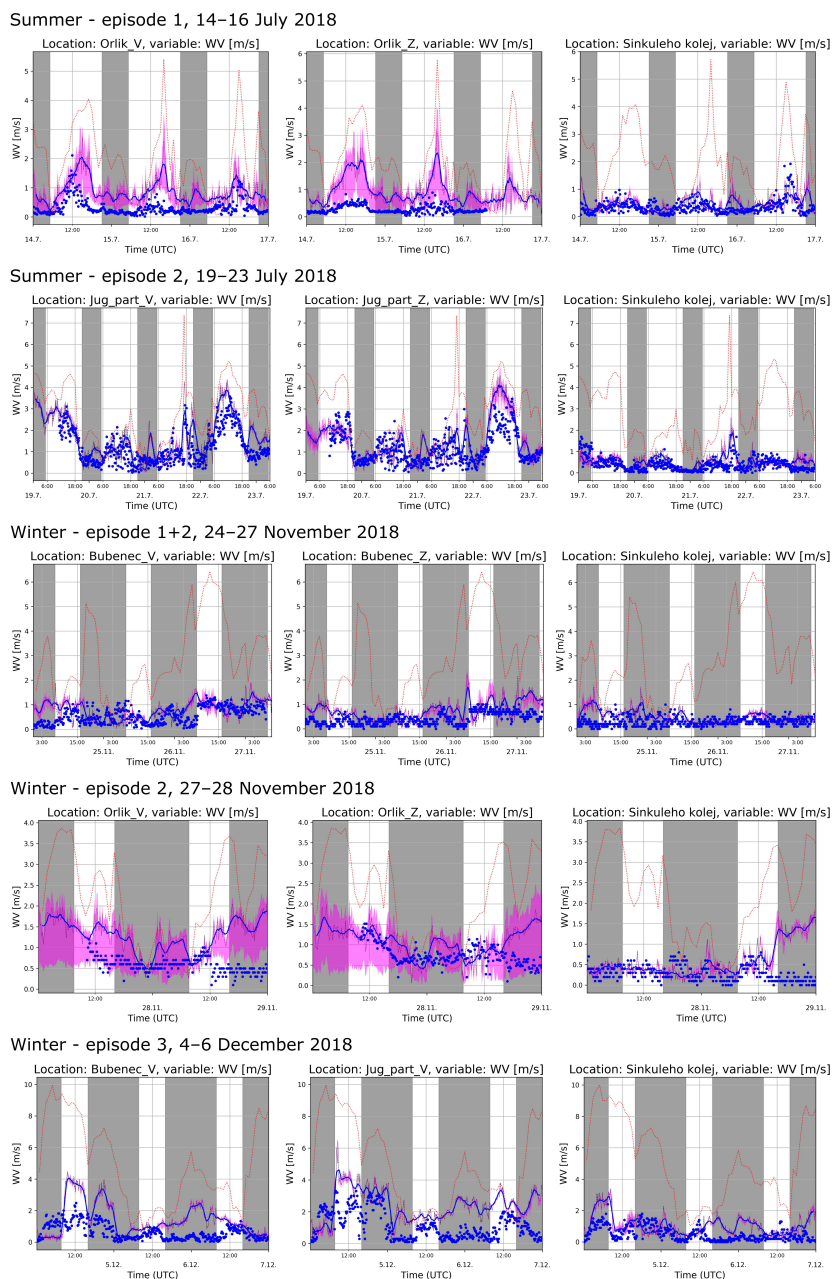


**Figure 33.** Modelled (solid blue line) and observed (blue dots) wind speed in particular street canyon observation locations. Solid blue line represents one-hour moving average while the darker magenta line shows the original 10-minutes averages. The light magenta band shows the interval between the smallest and the largest 10-minute average value among the neighbouring grid points. The thin dotted red line indicates corresponding value from WRF simulation.

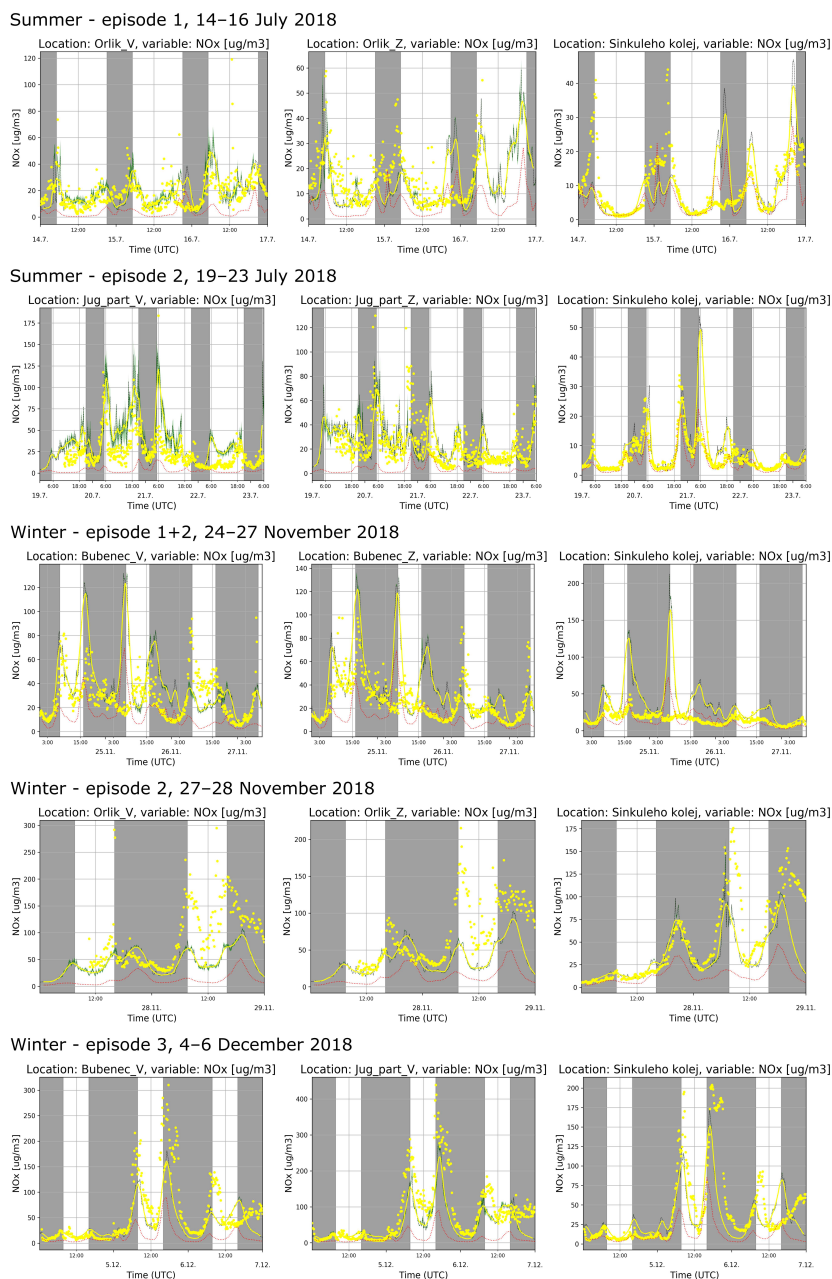


**Figure 34.** Graphs of NO<sub>x</sub> concentrations in street-canyon measuring locations. Yellow symbols denote observed 10-minute concentration averages, the black curve 10-minute concentration averages computed by PALM and the yellow curve 1-hour moving concentration averages computed by PALM. The light green band shows the interval between the smallest and the largest 10-minute average value among the neighbouring grid points. The red curve denotes the 1-hour concentration averages at the closest CAMx grid point.



**Table 2.** The model performance evaluation metrics according to Britter and Schatzmann (2007) and Chang and Hanna (2004) computed from 10-minute average concentrations of NO<sub>x</sub> modelled by PALM.

	summer	winter
N	3,039	3,816
mean obs [g.m <sup>-3</sup> ]	15.9	48.3
mean mod [g.m <sup>-3</sup> ]	19.0	38.9
FB	-0.18	0.21
NMSE	0.85	2.88
FAC2	0.69	0.64
R	0.59	0.63

N is the ensemble size, mean obs is the observed mean concentration, mean mod is the modelled mean concentration, FB is the fractional bias, NMSE the normalized mean square error, FAC2 is the fraction of predictions within a factor of two of the observations and R is the correlation coefficient.

In addition to the stationary measurements, mobile observations of the air quality indicators were performed (see Sect. 2.3.4 for details). Here we compare modelled values in grid points corresponding to the position of the mobile instruments for NO<sub>x</sub> (Fig. 35; for PM<sub>10</sub> see Fig. S24 in the supplement). For the summer episode (19 July) the morning measurements are shown.

825 The observed values show quite high variability within the short timeframe of the measurement in many location (variability between 20–160 μg.m<sup>-3</sup>). On the other hand, the oscillations are very small during some other measurements (e.g. loc. 6–17 on 19 July or partly loc. 13 on 4 December). This high variability of some measured values suggests impact of a very close local source of emission (e.g. bus on bus station or local heating) which, however, cannot be verified with the data available. Moreover, these oscillations are not present in the PM<sub>10</sub> observations, which supports the aforementioned hypothesis of local  
830 NO<sub>x</sub> sources in contrast to dynamical causes.

In the winter episode, on 4 December observations show much higher variability than in the summer episode. During the morning series modelled values correspond well with measurements for the most part with the exception of the measurement point 11 in which the model is 2–5 times lower. The afternoon series shows good agreement in points 2, 3, 4, 13 and 14. In points 10 and 11 the model results are again consistently lower than in reality.

## 835 5 Summary and conclusions

### 5.1 Summary of the results

In this study, PALM LES simulations nested into the mesoscale WRF and CAMx simulations were performed for a real urban environment in Prague-Dejvice, Czech Republic. Meteorological, air quality and wall-surface quantities were compared against in-situ measurements taken during a specially designed observation campaign. Air temperature, wind speed and chemical  
840 concentrations agreed well with the observations with respect to their temporal evolution and daily amplitude, except for the observed strong nighttime cooling on 15 July, 20 July, and 21 July, which was not well captured by the LES, probably due to a

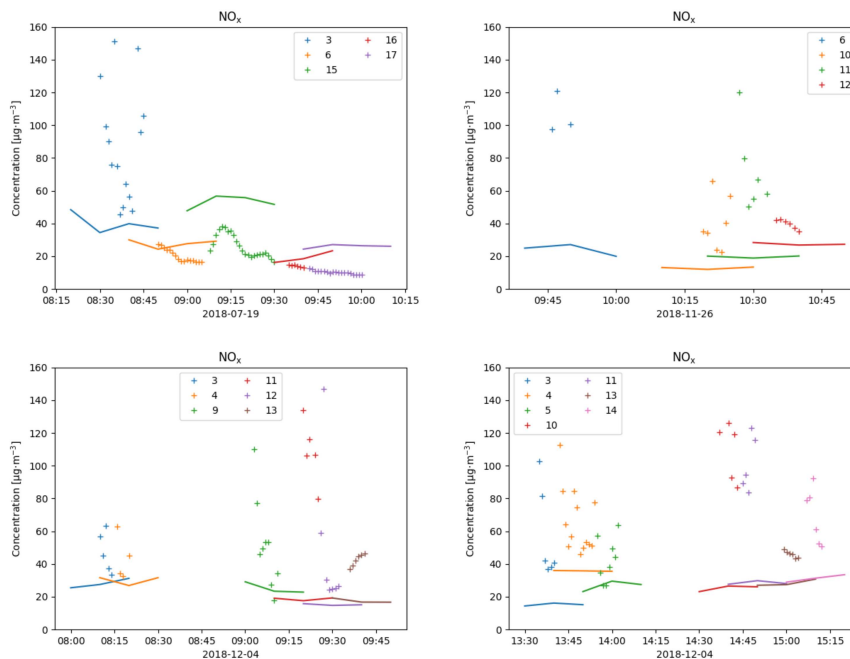


**Figure 35.** Mobile  $\text{NO}_x$  measurements (+ marker) and modelled concentrations (solid) for 19 July 2018 morning (top left), 26 November morning (top right), 4 December 2018 morning (bottom left) and 4 December 2018 afternoon (bottom right).

misrepresentation of the stable conditions. This issue needs further investigation in the future. The modelled street-canyon air temperature and wind speed agree well with the observations and properly adjusts to the temporally evolving WRF conditions. However, the modelled wind speed shows higher values compared to the observed one for location Orlik in some time periods, which can be explained by large spatial gradients near the buildings and by the tree crowns which are partly too small in the model. Further, especially during the winter episodes, meteorological quantities resemble the simulated WRF values due to a weaker local energy forcing, meaning that the accuracy of the model results is strongly related to WRF accuracy.

Concentrations of  $\text{NO}_x$  were modelled well in some situations and PALM properly supplies the local air pollution to the urban background values provided by CAMx simulation while for some places and times (mainly about sunset or sunrise) it overpredicts the concentrations of  $\text{NO}_x$  (e.g. 15 July evening, 25 November morning). That is probably related to atmospheric stability and uncertainties of modelling stably stratified turbulent flow. The opposite situation (i.e. the underpredicting of  $\text{NO}_x$ ) occurs less often (e.g. during the night from 14 July to 15 July). These discrepancies could be partially connected with uncertainties of the emission and with imperfection in WRF and CAMx provided boundary conditions but a more probable cause is the deviation of the PALM modelled turbulent flow under some meteorological conditions. This issue needs further investigation.

The modelled surface temperature agrees well with the observed one at most of the surface evaluation points. However, it strikes that the agreement is usually better for the summer episodes when strong radiative forcing exists than for the winter



episodes when the model results are more prone to uncertain material properties as well as inaccuracies with respect to the atmospheric conditions given by the mesoscale model. The surface temperature at pavement surfaces and at wall surfaces belonging to traditional buildings built e.g. from bricks or building blocks, is usually modelled well, while the surface temperature at modern buildings with multi-layer prefabricated walls is less well captured.

At natural ground surfaces the modelled surface temperature agrees also well with the observation, even though we note that the model results strongly depend on a proper description of initial soil moisture and properly other surface-material parameters. Beside an accurate prescription of surface-material parameters, also an accurate representation of the LAD is essential for accurate modelling of the local atmosphere-surface exchange. Even though this study contains some indicative sensitivity investigations for the studied domain and episodes, we note that a systematic sensitivity study on the model input parameters is out of the scope of this paper and the reader is referred to Belda et al. (2020). Furthermore, issues related to the discrete representation of the terrain and building surfaces on the Cartesian grid revealed to be a crucial factor for model inaccuracy (see Sect. 4.3.5).

## 5.2 Outlook of model development and data improvement

This study also points towards particular aspects in the model, input data preparation and observation strategy that deserve particular focus in the future.

The current method of discretization of terrain and buildings in PALM is bound to the Cartesian model grid, which means that an entire volume of each grid cell contains either atmosphere (free or with plant canopy) or obstacle (terrain or building). As a result, every model surface forms a boundary between grid cells and its normal is parallel to one of the grid axes. If the modelled domain contains uneven terrain, sloped roofs or walls that are not parallel to the grid axes, e.g. facades that are aligned along the NE-SW direction, the discretization creates artificial steps which affect radiative fluxes as well as the airflow. For example, such step-like surfaces create artificial shading or sunlit surfaces modifying the energy balance on the microscale. Further, observation points cannot be assigned arbitrarily to the discrete grid any more, which in turn complicates the analysis for non-grid aligned facades. For such locations, the values of modelled variables may need further postprocessing, or may be even unsuitable for validation and a location further away from the step need to be used instead. Examples of these issues are presented in Section 4.3.5. A major change of discretization is planned for future versions of the PALM model – surfaces will be represented using the Immersed Boundary Method (see Peskin, 1972). This method allows to represent surfaces with arbitrary orientation, thus avoiding the creation of artificial steps.

In the current version of the RTM model, all surfaces are considered as Lambertian reflectors, meaning that directional reflection at windows or polished materials cannot be considered, which, however, can be found at almost every facade. This in turn adds uncertainty to the surface net radiation and thus to the energy balance at the surrounding surfaces. Implementation of specular reflection is planned to better simulate the radiative transfer at glass and polished surfaces.

The current implementation of the BSM discretizes walls by four layers, independent of the thickness or the material of the wall, meaning that the grid resolution of the wall layers may differ among different wall surfaces. Further, wall material properties at walls with multiple layers are sometimes not well considered by only four wall layers, leading e.g. to an under-



or overestimation of the thickness of the insulating layer. A variable number of wall layers would allow to represent wall material properties more realistically. Moreover, pre-prepared typical structures of the complex wall composition in BEM would simplify proper initialization of these walls.

895 The analysis of air and surface temperatures revealed insufficient cooling of the air during nights in certain meteorological conditions where the stratification is underestimated by the model. In this study we explicitly prescribe the incoming radiation where radiative cooling of the air volume itself is not considered. Hence, in order to check how sensitive the model results are on this, we also ran test simulations where we applied the RRTMG radiation scheme and where radiative cooling of the air volume is considered; however, we could observe similar insufficient cooling in this case. This insufficient cooling during  
900 nighttime requires further investigation in the future.

Another implication arises from the mesoscale nesting approach. The analysis of wind speeds at higher levels and temperatures revealed that PALM mostly reflects the conditions simulated by the mesoscale model (WRF), especially during wintertime. This in turn suggests that the model domain of the nested LES simulation might be too small to develop its own equilibrium. However, this needs further investigation in the future. Moreover, as the mesoscale simulation does not resolve the  
905 turbulent flow, we need to impose synthetic turbulence at the inflow boundaries. Even though the inflow is already turbulent, the turbulent flow needs to develop spatially downstream of the inflow boundary forming coherent structures which require significant large fetch lengths of several kilometers (Muñoz-Esparza et al., 2017; Lee et al., 2018). However, in the urban layer the adjustment is faster and 1-2 km are sufficient for the building-affected layer (Lee et al., 2018). Although the flow within the building-affected layer is well developed in the analysis area, the turbulent flow within the upper parts of the boundary layer  
910 has still not been fully developed. This implies that mixing processes at the boundary-layer top and its impact on near-surface microscale processes might be not considered well, though this was not the focus of this study.

The study suggests strong sensitivity of the results on accurate input data, e.g. for the wall-material properties. The sensitivity of the PALM model to the material parameters is more systematically investigated in Belda et al. (2020). Bulk parameters prescribed for certain building categories might strongly deviate from the actual conditions at the building. Hence, usage  
915 of bulk input parameters might significantly modify the simulation results locally. Other specific observations are needed to improve properties of the categories of wall, roofs, and pavement materials. The study also stresses the need for precise boundary conditions as well as correct setting of the initial soil moisture for natural surfaces.

The experimental campaign also serves as a source of useful experience for future studies of similar type. Modern buildings with high amounts of glass and other reflective surfaces on the surface proved to be challenging for surface temperature mea-  
920 surements using an IR camera. The reflections often hide the thermal radiation of the surface. A higher number of traditional buildings (bricks, concrete) would allow better assessment of the accuracy of the building surface parameterizations, which are primarily developed for these types of buildings and of the accuracy of the parameters assumed for these buildings. Data from mobile measurement vehicles proved to be difficult to interpret and difficult to draw statistically relevant conclusions from. In future, either a significantly higher number of measurements would be required or the effort should concentrate elsewhere. One  
925 of the directions to be considered is a combination of traditionally full-featured vehicle-observation stations with a network of the sensors. Further, drone measurements in a city are limited by various restrictions based by the air traffic control and land



owners. The whole city of Prague is located in controlled airspace that starts at the ground and our area of interest also lies in restricted airspace. A drone flight must be programmed with regard to the properties of the measurement sensors, e.g. the relaxation time, and preparatory test flights with the drone operator may be necessary. Regular aerological soundings from the Praha-Libuš station proved to be indispensable. In future, increasing the frequency of measurements during a measurement campaign would be very useful and the possibility of dedicated soundings in the area of interest should be considered.

*Code and data availability.* The PALM model system is freely available from <http://palm-model.org> (last access: 29 May 2020) and distributed under the GNU General Public Licence v3 (<http://www.gnu.org/copyleft/gpl.html>, last access: 29 May 2020). The model source code version 6.0 in revision r4508 used in this article is also available via <https://doi.org/10.25835/0073713> (Resler et al., 2020).

*Author contributions.* Coordination of the study, leading of UrbiPragensi KK4 concept: JR, coordination of the observation campaign: OV, design of the observation campaign: JKe, OV, JR, MB, realization of the observation campaign: OV, JR, JG, KE, PK, MB, VF, PH, JKa, JD, TH, KH, JKe, observation postprocessing: OV, KH, SN, JR, JG, PK, MR, MB, VF, urban input data collection and processing: JG, JR, PK, OV, NB, WRF and CAMx simulations and their processing: KE, PH, MB, JK, JR, PK, OV, NB, JD, PALM model development and testing: JR, MS, PK, VF, PALM simulations configuration and run: JR, MS, PK, result postprocessing and visualisation: JR, JG, MR, PK, MB, VF, meteorology and air quality expertise: MS, MB, VF, OV, PH, JKe, text contribution and revisions: all co-authors.

*Competing interests.* The authors declare no competing interests.

*Acknowledgements.* Financial support was provided by the *Operational Program Prague – Growth Pole of the Czech Republic* project “Urbanization of weather forecast, air-quality prediction and climate scenarios for Prague” (CZ.07.1.02/0.0/0.0/16\_040/0000383) which is co-financed by the EU. The co-author MS was supported by the Federal German Ministry of Education and Research (BMBF) under grant 01LP1601 within the framework of *Research for Sustainable Development (FONA)*<sup>1</sup>.

The terrain mapping campaign of building properties was co-financed by the *Strategy AV21* project “Energy interactions of buildings and the outdoor urban environment” which is financed by the Czech Academy of Sciences. We would like to thank prof. Jiří Cajthaml and students of the Faculty of Civil Engineering of the Czech Technical University in Prague for their help with the terrain mapping campaign.

We would also like to thank to the Global Change Research Institute (CzechGlobe) for lending the IR camera, Ms. Ivana Hájíčková for enabling the HF measurements in Zelená St., and the Czech Technical University (Ms. Lenka Bedrníková and Mr. Josef Šteffel) for enabling us to perform the heat flux measurement at Sinkule house and the wind measurements on the rooftop of the Faculty of Civil Engineering of CTU.

---

<sup>1</sup><https://www.fona.de>



We would like to thank our colleagues, who organised and carried out the measurements during the observation campaign and are not authors of this article. Monitoring vehicles - Zdeněk Běťák, Petr Goll, Jan Kufel, Luboš Vrána; mobile and rooftop wind measurement -  
955 Petra Bauerová, Jan Hadinger, Zdeněk Proškovec, Hana Škáchová; IR measurements - Jana Řadová, Michal Žák; technician - Jiří Gajdoš.

The PALM simulations, pre- and postprocessing were performed on the HPC infrastructure of the Institute of Computer Science of the Czech Academy of Sciences (ICS) supported by the long-term strategic development financing of the ICS (RVO:67985807). Part of the simulations were performed on the supercomputer of the Czech supercomputing centre IT4I which was supported by The Ministry of Education, Youth and Sports from the *Large Infrastructures for Research, Experimental Development and Innovations* project “IT4Innovations National  
960 Supercomputing Center — LM2015070” and on the supercomputers of the North-German Supercomputing Alliance (HLRN). The WRF and CAMx simulations were done on the HPC infrastructure of the Department of Atmospheric Physics of the Faculty of Mathematics and Physics of the Charles University in Prague which was supported by the *Operational Program Prague – Growth Pole of the Czech Republic* project “Urbanization of weather forecast, air-quality prediction and climate scenarios for Prague” (CZ.07.1.02/0.0/0.0/16\_040/0000383) which is co-financed by the EU.



## 965 References

- Belda, M., Eben, K., Fuka, V., Geletič, J., Kanani-Sühring, F., Krč, P., Maronga, B., Resler, J., Benešová, N., Sühring, M., Auvinen, M., and Kurppa, M.: Sensitivity analysis of the PALM model system 6.0 in the urban environment, submitted to Geosci. Model. Dev., 2020.
- Bougeault, P. and Lacarrère, P.: Parameterization of Orography-Induced Turbulence in a Mesobeta-Scale Model, *Mon. Wea. Rev.*, 117, 1872–1890, [http://dx.doi.org/10.1175/1520-0493\(1989\)117<1872:POOITI>2.0.CO;2](http://dx.doi.org/10.1175/1520-0493(1989)117<1872:POOITI>2.0.CO;2), 1989.
- 970 Briscolini, M., and Santangelo, P.: Development of the mask method for incompressible unsteady flows, *J. Comp. Phys.*, 84, 57–75, [https://doi.org/10.1016/0021-9991\(89\)90181-2](https://doi.org/10.1016/0021-9991(89)90181-2), 1989.
- Britter, R., and Schatzmann, M.: Model Evaluation Guidance and Protocol Document, COST Office Brussels, Brussels/Belgium, 28 p., ISBN 3-00-018312-4, 2007.
- Brugger, P., Banerjee, T., De Roo, F., Kröniger, K., Qubaja, R., Rohatyn, S., Rotenberg, E., Tatarinov, F., Yakir, D., Yang, F., and Mauder, M.: Effect of Surface Heterogeneity on the Boundary-Layer Height: A Case Study at a Semi-Arid Forest, *Boundary-Layer Meteorol.*, 169, 2, 233–250, <https://doi.org/10.1007/s10546-018-0371-5>, 2018.
- 975 Builtjes, P. J. H., van Loon, M., Schaap, M., Teeuwisse, S., Visschedijk, A. J. H., and Bloos, J. P.: Project on the modelling and verification of ozone reduction strategies: contribution of TNO-MEP. TNO-report, MEP-R2003/166, Apeldoorn, Netherlands, 2003.
- Byun, D. W.: Dynamically Consistent Formulations in Meteorological and Air Quality Models for Multiscale Atmospheric Studies. Part II: Mass Conservation Issues, *J. Atmos. Sci.*, 56, 3808–3820, [https://doi.org/10.1175/1520-0469\(1999\)056<3808:DCFIMA>2.0.CO;2](https://doi.org/10.1175/1520-0469(1999)056<3808:DCFIMA>2.0.CO;2), 1999.
- 980 Carslaw, D. C., and Ropkins, K.: openair – an R package for air quality data analysis, *Environmental Modelling & Software*, 27–28, 52–61, <https://doi.org/10.1016/j.envsoft.2011.09.008>, 2012.
- Chang, J., and Hanna, S.: Air quality model performance evaluation, *Meteorol. Atmos. Phys.*, 87, 167–196, <https://doi.org/10.1007/s00703-003-0070-7>, 2004.
- 985 Chen, F., and Dudhia, J.: Coupling an advanced land-surface/ hydrology model with the Penn State/ NCAR MM5 modeling system. Part I: Model description and implementation, *Mon. Wea. Rev.*, 129, 569–585, [https://doi.org/10.1175/1520-0493\(2001\)129<0569:CAALSH>2.0.CO;2](https://doi.org/10.1175/1520-0493(2001)129<0569:CAALSH>2.0.CO;2), 2001.
- Ching, J., Rotunno, R., LeMone, M., Martilli, A., Kosovic, B., Jimenez, P. A., and Dudhia, J.: Convectively Induced Secondary Circulations in Fine-Grid Mesoscale Numerical Weather Prediction Models, *Monthly Weather Review*, 142, 9, 3284–3302, <https://doi.org/10.1175/MWR-D-13-00318.1>, 2014.
- 990 ČHMÚ (Czech Hydrometeorological Institute): Measurements of air quality and micrometeorology in street canyons in Prague 6 – Dejvice, 2018. Campaign within the Urbi Pragensi project financed from the Operational Programme Prague – Growth Pole of the Czech Republic, project No. CZ.07.1.02/0.0/0.0/16\_040/0000383. ČHMÚ’s Technical document No. TD 000129, Prague, Czech Rep., 2020.
- 995 ČÚZK (Czech Office for Surveying, Mapping and Cadastre): GeoPortal Datasets (ZABAGED and orthophoto), 2020. Available at: [https://geoportal.cuzk.cz/\(S\(hwwp4jhepqmkrmonodglvjwu\)\)/Default.aspx?lng=EN&head\\_tab=sekce-02-gp&mode=TextMeta&text=dSady\\_uvod&menu=20](https://geoportal.cuzk.cz/(S(hwwp4jhepqmkrmonodglvjwu))/Default.aspx?lng=EN&head_tab=sekce-02-gp&mode=TextMeta&text=dSady_uvod&menu=20) (last access: May 2020)
- Deardorff, J. W.: Stratocumulus-capped mixed layers derived from a three-dimensional model, *Boundary-Layer Meteorol.*, 18, 495–527, <https://doi.org/10.1007/BF00119502>, 1980.



- 1000 Denier van der Gon, H., Hendriks, C., Kuenen, J., Segers, A., and Visschedijk, A.: Description of current temporal emission patterns and sensitivity of predicted AQ for temporal emission patterns. EU FP7 MACC deliverable report D\_D-EMIS\_1.3, 2011. Available at: [http://www.gmes-atmosphere.eu/documents/deliverables/d-emis/MACC\\_TNO\\_del\\_1\\_3\\_v2.pdf](http://www.gmes-atmosphere.eu/documents/deliverables/d-emis/MACC_TNO_del_1_3_v2.pdf).
- 1005 Ďoubalová, J., Huszár, P., Eben, K., Benešová, N., Belda, M., Vlček, O., Karlický, J., Geletič, J., and Halenka, T.: High resolution air quality forecasting over Prague within the Urbi Pragensi project: model performance during winter period and the effect of urban parameterization on PM. *Atmosphere*, in review, 2020.
- ENVIRON, CAMx User's Guide, Comprehensive Air Quality model with Extensions, version 6.50., [www.camx.com](http://www.camx.com), Novato, California, 2018.
- FLIR: FLIR SC660 R and D INFRARED CAMERA SYSTEM. Product leaflet, 2008. Available at: <https://www.flir.com/products/t660/> (last access: May 2020)
- 1010 Fröhlich, D., and Matzarakis, A.: Calculating human thermal comfort and thermal stress in the PALM model system 6.0, *Geosci. Model Dev. Discuss.*, 2019, 1–21, <https://doi.org/10.5194/gmd-2019-202>, 2019.
- Gehrke, K. F., Sühling, M., van Heerwaarden, C., and Maronga, B.: Modeling of land-surface interactions in the PALM model system 6.0: Land surface model description and evaluation against in-situ measurement data in Cabauw, submitted to *Geosci. Model Dev.*, 2020.
- Geletič, J., Lehnert, M., Savić, S., and Milošević, D.: Modelled spatiotemporal variability of outdoor thermal comfort in local climate zones of the city of Brno, Czech Republic, *Sci. Tot. Environ.*, 624, 385–395, <https://doi.org/10.1016/j.scitotenv.2017.12.076>, 2018.
- 1015 Hong, S.-Y., Noh, Y., and Dudhia, J.: A new vertical diffusion package with an explicit treatment of entrainment processes, *Mon. Wea. Rev.*, 134, 2318–2341, <https://doi.org/10.1175/MWR3199.1>, 2006.
- Heldens, W., Burmeister, C., Kanani-Sühling, F., Maronga, B., Pavlik, D., Sühling, M., Zeidler, J., and Esch, T.: Geospatial input data for the PALM model system 6.0: model requirements, data sources, and processing, *Geosci. Model Dev. Discuss.*, <https://doi.org/10.5194/gmd-2019-355>, in review, 2020.
- 1020 Hellsten, A., Ketelsen, K., Raasch, S., Maronga, B., Sühling, M., Knigge, C., Barmpas, F., Tsegas, G., Auvinen, M., and Moussiopoulos, N.: A Nested Multi-Scale System Implemented in the Large-Eddy Simulation Model PALM, to be submitted to *Geosci. Model Dev.*, 2020.
- Hukseflux, 2020. TRSYS01 heat flux measuring system. Available at: <https://www.hukseflux.com/products/heat-flux-sensors/heat-flux-measuring-systems/trsys01-heat-flux-measuring-system> (last access: May 2020)
- 1025 Huszár, P., Karlický, J., Belda, M., Halenka, T., and Pišoft, P.: The impact of urban canopy meteorological forcing on summer photochemistry, *Atmos. Environ.*, 176, 209–228, <https://doi.org/10.1016/j.atmosenv.2017.12.037>, 2018a.
- Huszár, P., Belda, M., Karlický, J., Bardachová, T., Halenka, T., and Pišoft, P.: Impact of urban canopy meteorological forcing on aerosol concentrations, *Atmos. Chem. Phys.*, 18, 14059–14078, <https://doi.org/10.5194/acp-18-14059-2018>, 2018b.
- Huszár, P., Karlický, J., Ďoubalová, J., Šindelářová, K., Nováková, T., Belda, M., Halenka, T., Žák, M., and Pišoft, P.: Urban canopy meteorological forcing and its impact on ozone and PM<sub>2.5</sub>: role of vertical turbulent transport, *Atmos. Chem. Phys.*, 20, 1977–2016, <https://doi.org/10.5194/acp-20-1977-2020>, 2020.
- 1030 Iacono, M. J., Delamere, J. S., Mlawer, E. J., Shephard, M. W., Clough, S. A., and Collins, W. D.: Radiative forcing by long-lived greenhouse gases: Calculations with the AER radiative transfer models, *J. Geophys. Res.*, 113, D13103, 2–9, <https://doi.org/10.1029/2008JD009944>, 2008.
- 1035 IPCC: Climate Change 2014: Impacts, Adaptation, and Vulnerability. Part A: Global and Sectoral Aspects. Contribution of Working Group II to the Fifth Assessment Report of the Intergovernmental Panel on Climate Change, edited by: Field, C. B., Barros, V. R., Dokken, D. J., Mach, K. J., Mastrandrea, M. D., Bilir, T. E., Chatterjee, M., Ebi, K. L., Estrada, Y. O., Genova, R. C., Girma, B., Kissel, E. S., Levy, A.



- N., MacCracken, S., Mastrandrea, P. R., and White, L. L., Cambridge University Press, Cambridge, United Kingdom and New York, NY, USA, 1132 pp., <https://doi.org/10.1017/CBO9781107415379>, 2014a.
- 1040 IPCC: Climate Change 2014: Mitigation of Climate Change. Contribution of Working Group III to the Fifth Assessment Report of the Intergovernmental Panel on Climate Change, edited by: Edenhofer, O., Pichs-Madruga, R., Sokona, Y., Farahani, E., Kadner, S., Seyboth, K., Adler, A., Baum, I., Brunner, S., Eickemeier, P., Kriemann, B., Savolainen, J., Schlömer, S., von Stechow, C., Zwickel, T., and Minx, J. C., Cambridge University Press, Cambridge, United Kingdom and New York, NY, USA, <https://doi.org/10.1017/CBO9781107415416>, 2014b.
- 1045 Kadasch, E., Sühling, M., Gronemeier, T., and Raasch, S.: Offline nesting of the large-eddy simulation model PALM 6.0 in a mesoscale model, in preparation, to be submitted to Geosci. Model Dev., 2020.
- Khan, B., Forkel, R., Banzhaf, S., Mauder, M., Chan, E. C., Russo, E., Sühling, M., Kurppa, M., Kanani-Sühling, F., Maronga, B., Schaap, M., Raasch, S., and Ketelsen, K.: Development and Application of an Atmospheric Chemistry Model to the Urban Micro-scale Modelling System PALM-4U, in preparation, to be submitted to GMD, to be submitted to Geosci. Model Dev., 2020.
- 1050 Krč, P., Resler, J., Fuka, V., Sühling, M., Salim, M., and Schubert, S.: Radiative Transfer Model 3.0 integrated into the PALM model system 6.0. Submitted to Geosci. Model Dev., 2020.
- Lee, G.-J., Muñoz-Esparza, D., Yi, Ch., and Choe, H. J.: Application of the Cell Perturbation Method to Large-Eddy Simulations of a Real Urban Area, *J. Appl. Meteor. Climatol.*, 58, 5, 1125–1139, <https://doi.org/10.1175/JAMC-D-18-0185.1>, 2018.
- 1055 Lemonsu, A., Bélair, S., Mailhot, J., Benjamin, M., Morneau, G., Harvey, B., Chagnon, F., Jean, M., and Voogt, J.: Overview and First Results of the Montreal Urban Snow Experiment 2005, *J. Appl. Meteor. Climatol.*, 47, 59–75, <https://doi.org/10.1175/2007JAMC1639.1>, 2008.
- Liu, Y. S., Miao, S. G., Zhang, C. L., Cui, G. X., and Zhang, Z. S.: Study on micro-atmospheric environment by coupling large eddy simulation with mesoscale model, *J. Wind Eng. Indust. Aerodyn.*, 107–108, 106–117, <https://doi.org/10.1016/j.jweia.2012.03.033>, 2012.
- 1060 Maggioletto, G., Buccolieri, R., Santo, M. A., Leo, L. S., and Di Sabatino, S.: Validation of temperature-perturbation and CFD-based modelling for the prediction of the thermal urban environment, *Environ. Model. Softw.*, 60, 69–83, <https://doi.org/10.1016/j.envsoft.2014.06.001>, 2014.
- Maronga, B., Gryschka, M., Heinze, R., Hoffmann, F., Kanani-Sühling, F., Keck, M., Ketelsen, K., Letzel, M. O., Sühling, M., and Raasch, S.: The Parallelized Large-Eddy Simulation Model (PALM) version 4.0 for atmospheric and oceanic flows: model formulation, recent developments, and future perspectives, *Geosci. Model Dev.*, 8, 2515–2551, <https://doi.org/10.5194/gmd-8-2515-2015>, 2015.
- 1065 Maronga, B., Banzhaf, S., Burmeister, C., Esch, T., Forkel, R., Fröhlich, D., Fuka, V., Gehrke, K. F., Geletič, J., Giersch, S., Gronemeier, T., Groß, G., Heldens, W., Hellsten, A., Hoffmann, F., Inagaki, A., Kadasch, E., Kanani-Sühling, F., Ketelsen, K., Khan, B. A., Knigge, C., Knoop, H., Krč, P., Kurppa, M., Maamari, H., Matzarakis, A., Mauder, M., Pallasch, M., Pavlik, D., Pfafferoth, J., Resler, J., Rissmann, S., Russo, E., Salim, M., Schrempf, M., Schwenkel, J., Seckmeyer, G., Schubert, S., Sühling, M., von Tils, R., Vollmer, L., Ward, S., Witha, B., Wurps, H., Zeidler, J., and Raasch, S.: Overview of the PALM model system 6.0, *Geosci. Model Dev.*, 13, 1335–1372, <https://doi.org/10.5194/gmd-13-1335-2020>, 2020.
- 1070 Masson, V., Gomes, L., Pigeon, G., Liousse, C., Pont, V., Lagouarde, J.-P., Voogt, J., Salmond, J., Oke, T. R., Hidalgo, J., Legain, D., Garrouste, O., Lac, C., Connan, O., Briottet X., and Lachéradé, S.: The Canopy and Aerosol Particles Interactions in TOulouse Urban Layer (CAPITOU) experiment, *Meteorol. Atmos. Phys.*, 102, 3–4, 135–157, <https://doi.org/10.1007/s00703-008-0289-4>, 2008.



- 1075 Masson, V., Heldens, W., Bocher, E., Bonhomme, M., Bucher, B., Burmeister, C., deMunck, C., Esch, T., Hidalgo, J., Kanani-Sühring, F.,  
and Kwok, Y. T.: City-descriptive input data for urban climate models: model requirements, data sources and challenges, *Urban Clim.*,  
31, 100536, <https://doi.org/10.1016/j.uclim.2019.100536>, 2020.
- Mazzaro, L. J., Muñoz-Esparza, D., Lundquist, J. K., and Linn, R. R.: Nested mesoscale-to-LES modeling of the atmospheric boundary  
layer in the presence of under-resolved convective structures, *Journal of Advances in Modeling Earth Systems*, 9, 4, 1795–1810, <https://doi.org/10.1002/2017MS000912>, 2017.
- 1080 Moeng, C.-H., and Wyngaard, J. C.: Spectral analysis of large-eddy simulations of the convective boundary layer, *J. Atmos. Sci.*, 45,  
3573–3587, [https://doi.org/10.1175/1520-0469\(1988\)045<3573:SAOLES>2.0.CO;2](https://doi.org/10.1175/1520-0469(1988)045<3573:SAOLES>2.0.CO;2), 1988.
- Möttus, M., Sulev, M., Lang, M., and Wyngaard, J. C.: Estimation of crown volume for a geometric radiation model from detailed measure-  
ments of tree structure, *Ecological Modelling*, 198, 3–4, 506–514, <https://doi.org/10.1016/j.ecolmodel.2006.05.033>, 2006.
- Muñoz-Esparza, D., Lundquist, J. K., Sauer, J. A., Kosović, B., and Linn, R. R.: Coupled mesoscale-LES modeling of a diurnal cycle during  
1085 the CWEX -13 field campaign: From weather to boundary-layer eddies, *J. Adv. Model. Earth Syst.*, 9, 1572–1594, <https://doi.org/10.1002/2017MS000960>, 2017.
- Mutani, G., and Fiermonte, F.: Microclimate models for a sustainable and liveable urban planning. In: Ingaramo, R., Voghera, A.  
(Eds.), *Topics and Methods for Urban and Landscape Design*, Springer International Publishing, 183–209, <https://doi.org/10.1007/978-3-319-51535-9>, 2017.
- 1090 Nenes, A., Pandis, S. N., and Pilinis, C.: ISORROPIA: a new thermodynamic equilibrium model for multiphase multicomponent inorganic  
aerosols, *Aquat. Geochem.*, 4, 123–152, <https://doi.org/10.1023/A:1009604003981>, 1998.
- Novák, J., Jiřina, M., and Benešová, M.: Projekt TDD–ČR, Popis modelu TDD verze 3.9, Výzkumná zpráva č. V-1261, Ústav Informatiky AV  
ČR, v.v.i., Prague, Czech Republic, 2019. Available at: [https://www.ote-cr.cz/en/documentation/gas-documentation/tdd-documentation?](https://www.ote-cr.cz/en/documentation/gas-documentation/tdd-documentation?set_language=en)  
set\_language=en (last access: May 2020)
- 1095 Nozu, T., Tamura, T., Okuda, Y., and Sanada, S.: LES of the flow and building wall pressures in the center of Tokyo, *J. Wind Eng. Indust.  
Aerodyn.*, 96, 1762–1773, <https://doi.org/10.1016/j.jweia.2008.02.028>, 2008.
- OTE: Normalizované typové diagramy dodávek plynu, 2020. Available at: <https://www.ote-cr.cz/cs/statistika/typove-diagramy-dodavek-plynu/normalizovane-tdd> (last access: May 2020).
- Peskin, C. S.: Flow patterns around heart valves: A numerical method, *J. Comput. Phys.*, 10, 2, 252–271, [https://doi.org/10.1016/0021-9991\(72\)90065-4](https://doi.org/10.1016/0021-9991(72)90065-4), 1972.
- 1100 Prague Geoportal: Prague geographic data in one place, 2020. Available at: <https://www.geoportalpraha.cz/en> (last access: May 2020)
- Qu, Y., Milliez, M., Musson-Genon, L., and Carissimo, B.: 3D Radiative and Convective Modeling of Urban Environment: An Ex-  
ample for the City Center of Toulouse. In: Steyn D., Builtjes P., Timmermans R. (eds) *Air Pollution Modeling and its Application  
XXII. NATO Science for Peace and Security Series C: Environmental Security*. Springer, Dordrecht, 727–731, [https://doi.org/10.1007/978-94-007-5577-2\\_123](https://doi.org/10.1007/978-94-007-5577-2_123), 2013.
- 1105 R Core Team: R: A language and environment for statistical computing. R Foundation for Statistical Computing, Vienna, Austria. <https://www.R-project.org/>, 2019.
- Resler, J., Krč, P., Belda, M., Juruš, P., Benešová, N., Lopata, J., Vlček, O., Damašková, D., Eben, K., Derbek, P., Maronga, B., and Kanani-  
Sühring, F.: PALM-USM v1.0: A new urban surface model integrated into the PALM large-eddy simulation model. *Geosci. Model Dev.*,  
1110 10, 3635–3659, <https://doi.org/10.5194/gmd-10-3635-2017>, 2017.
- Dataset: PALM 6.0 revision 4508. <https://doi.org/10.25835/0073713>, 2020.



- 1115 Rotach, M. W., Vogt, R., Bernhofer, C., Batchvarova, E., Christen, A., Clappier, A., Feddersen, B., Gryning, S-E., Martucci, G., Mayer, H., Mitev, V., Oke, T. R., Parlow, E., Richner, H., Roth, M., Roulet, Y-A., Ruffieux, D., Salmond, J. A., Schatzmann, M., and Voogt, J. A.: BUBBLE - an urban boundary layer meteorology project. *Theor. Appl. Climatol.*, 81, 3–4, 231–261, <https://doi.org/10.1007/s00704-004-0117-9>, 2005.
- ROTRONIC: HC2A-S - Humidity Probe, 2020. Available at: <https://www.rotronic.com/en/hc2a-s.html> (last access: May 2020).
- Saiki, E. M., Moeng, C.-H., and Sullivan, P. P.: Large-eddy simulation of the stably stratified planetary boundary layer, *Bound. Lay.-Meteorol.*, 95, 1–30, <https://doi.org/10.1023/A:1002428223156>, 2000.
- Seinfeld, J. H., and Pandis, S. N.: *Atmospheric Chemistry and Physics: From Air Pollution to Climate Change*. J. Wiley, New York, 1152 p., 1998. ISBN: 978-1-118-94740-1.
- 1120 Shaded Relief geoportal: Terrain, maps, and more, 2020. Available at: <http://www.shadedrelief.com> (last access: May 2020).
- Skamarock, W. C., Klemp, J. B., Dudhia, J., Gill, D. O., Barker, D., Duda, M. G., Huang, X.-Y., Wang, W., and Powers, J. G.: A Description of the Advanced Research WRF Version 3 (No. NCAR/TN-475+STR). University Corporation for Atmospheric Research. <http://dx.doi.org/10.5065/D68S4MVH>, 2008.
- 1125 Stewart, I. D., and Oke, T. R.: Local climate zones for urban temperature studies, *Bull. Amer. Meteor. Soc.*, 93, 1879–1900, <https://doi.org/10.1175/BAMS-D-11-00019.1>, 2012.
- Strader, R. Lurmann, F., and Pandis, S. N.: Evaluation of secondary organic aerosol formation in winter. *Atmos. Environ.*, 33, 4849–4863, [https://doi.org/10.1016/S1352-2310\(99\)00310-6](https://doi.org/10.1016/S1352-2310(99)00310-6), 1999.
- Toparlar, Y., Blocken, B., Vos, P., van Heijst, G. J. F., Janssen, W. D., van Hooff, T., Montazen, H., and Timmermans, H. J. P.: CFD simulation and validation of urban microclimate: a case study for Bergpolder Zuid, Rotterdam, *Build Environ.*, 83, 79–90, <https://doi.org/10.1016/j.buildenv.2014.08.004>, 2015.
- 1130 TSK-ÚDI: Prague Transportation Yearbook 2017, 2018. <http://www.tsk-praha.cz/static/udi-rocenka-2017-en.pdf> (last access: 11 May 2020).
- United Nations, Department of Economic and Social Affairs, Population Division: *World Urbanization Prospects: The 2018 Revision*, New York, 126 p. 2019. ISBN 978-92-1-148319-2.
- 1135 Wicker, L. J., and Skamarock, W. C.: Time-Splitting Methods for Elastic Models Using Forward Time Schemes, *Mon. Wea. Rev.*, 130, 2088–2097, [https://doi.org/10.1175/1520-0493\(2002\)130<2088:TSMFEM>2.0.CO;2](https://doi.org/10.1175/1520-0493(2002)130<2088:TSMFEM>2.0.CO;2), 2002.
- Williamson, J. H.: Low-storage Runge-Kutta schemes, *J. Comput. Phys.*, 35, 1, 48–56, [https://doi.org/10.1016/0021-9991\(80\)90033-9](https://doi.org/10.1016/0021-9991(80)90033-9), 1980.
- Xie, Z.-T., and Castro, I. P.: Efficient Generation of Inflow Conditions for Large Eddy Simulation of Street-Scale Flows, *Flow Turbul. Combust.*, 81, 449–470, <https://doi.org/10.1007/s10494-008-9151-5>, 2008.
- 1140 Yarwood, G., Rao, S., Yocke, M., and Whitten, G. Z.: Updates to the Carbon Bond chemical mechanism: CB05, Final Report prepared for US EPA, [http://www.camx.com/publ/pdfs/CB05\\_Final\\_Report\\_120805.pdf](http://www.camx.com/publ/pdfs/CB05_Final_Report_120805.pdf), Novato, NC, USA, 2005.
- Zhang, L., Brook, J. R., and Vet, R.: A revised parameterization for gaseous dry deposition in air-quality models, *Atmos. Chem. Phys.*, 3, 2067–2082, <https://doi.org/10.5194/acp-3-2067-2003>, 2003.
- Zhou, B., Simon, J. S., and Chow, F. K.: The Convective Boundary Layer in the Terra Incognita, *Journal of the Atmospheric Sciences*, 71, 7, 2545–2563, <https://doi.org/10.1175/JAS-D-13-0356.1>, 2014.
- 1145